Smoothed floating node method for modelling 2D arbitrary crack propagation problems

Singh, Umed; Kumar, Sachin; Chen, Boyang

DOI
10.1016/j.tafmec.2021.103190

Publication date
2022

Document Version
Final published version

Published in
Theoretical and Applied Fracture Mechanics

Theoretical and Applied Fracture Mechanics 117 (2022) 103190

Contents lists available at ScienceDirect

Theoretical and Applied Fracture Mechanics

journal homepage: www.elsevier.com/locate/tafmec

Smoothed floating node method for modelling 2D arbitrary crack propagation problems

Umed Singh [a], Sachin Kumar [a,*], Boyang Chen [b]

[a] Department of Mechanical Engineering, Indian Institute of Technology Ropar, Punjab 140001, India
[b] Faculty of Aerospace Engineering, Delft University of Technology, Netherlands

ARTICLE INFO

Keywords:
Floating node method
Smoothed finite element method
Smoothing domain
Stress intensity factors
Line integration

ABSTRACT

In this work, Floating Node Method (FNM), first developed for fracture modelling of laminate composites, is coupled with cell-wise strain Smoothed Finite Element Method (SFEM) for modelling 2D linear elastic fracture mechanics problems. The proposed method is termed as Smoothed Floating Node Method (SFNM). In this framework, FNM is used to represent the kinematics of crack and the crack front inside the domain without the requirement of remeshing and discontinuous enrichment functions during crack growth. For smoothing, a constant smoothing function is considered over the smoothing domains through which classical domain integration changes to line integration along each boundary of the smoothing cell, hence derivative of shape functions are not required in the computation of the field gradients. The values of stress intensity factor are obtained from the SFNM solution using domain based interaction integral approach. Few standard fracture mechanics problems are considered to check the accuracy and effectiveness of the proposed method. The predictions obtained with the proposed framework improves the convergence and accuracy of the results in terms of the stress intensity factors and energy norms.

1. Introduction

Defects such as cracks and voids are inevitable in the engineering materials and are mainly responsible for the fracture and failure of materials during the service. It is significant to study the amalgamation of the inherent micro cracks and voids, crack initiation and propagation of cracks in the structural components to predict the life span. The Finite Element Method (FEM) can be the best suited numerical tool to carry out such simulations of fracture mechanics problems. In FEM, mapped element takes part as a paired set between physical and natural coordinate system to maintain the exact equivalence. Thus, element distortion is not permitted as it causes singularity in the inversion of the stiffness matrix. Moreover, in simulations of crack propagation behaviour using FEM, conformal meshing is required to capture the crack discontinuity [1]. This mesh update in the crack tip vicinity corresponding to crack growth makes the simulation complex and time-consuming. In addition to this, remeshing during crack growth introduces error while shifting the field variables data from the previous mesh to the new one. Therefore, it becomes cumbersome to model crack propagation and evolving discontinuity using FEM approach alone. A more robust framework is desirable for the prediction of progressive failure. To this end, efforts have been made by researchers to establish different advanced numerical methods, such as the meshfree method [2–3], extended finite element method [4–6], phantom node method [7–8], boundary element method [9–10], isogeometric analysis [11–12], floating node method [13–14], continuum damage models [15–18], phase field method [19–21] etc. In this paper, we focus mainly on the discrete modelling approaches, hence only the ones closely related to this work are reviewed in the following paragraphs.

The detailed concepts of meshfree methods and their implementation aspects can be found in literature [22–23]. Meshfree methods have emerged as an alternative numerical method to alleviate the shortcomings related to conformal mesh requirement and element distortion in FEM. In meshfree methods, nodes are scattered inside the problem domain as well as on the boundary of the domain [24–26], and the nodal distribution density can be managed as per the requirement. The field variable is approximated at a point by considering the local support nodes surrounding the point of interest. The local support domain shape and size are not having a standard methodology but are user-dependent [27–29]. Usually, circular and rectangular shaped local supports are considered for the computation of field variables. Each integration domain is associated with a particular node and using one integration

* Corresponding author.
E-mail address: sachin@iitrpr.ac.in (S. Kumar).

https://doi.org/10.1016/j.tafmec.2021.103190
Received 20 October 2021; Received in revised form 19 November 2021; Accepted 19 November 2021
Available online 23 November 2021

point for the domain, equivalent to the reduced integration technique in FEM, may cause instability due to the higher order shape functions [30]. In practice, a very high number of Gauss points are required for integration, which makes it computationally expensive.

Another versatile approach to alleviate the FEM shortcomings is the Extended Finite Element Method (XFEM) wherein partition of unity property is incorporated [31–32]. In XFEM, crack discontinuity problems have been solved considering the displacement jump across the discontinuity by locally adding the enrichment functions to FEM approximation. In XFEM, a level set technique is used to capture the evolution of the discontinuity in the domain, which omits the requirement of remeshing [33–34]. This method has since been extended for fatigue crack growth [35], interfacial crack [36], elasto-plastic crack growth [37–39], dynamic crack growth [40], and functionally graded materials [41–43] etc. Despite its success, there exists some limitations i.e. it introduces an error in the solution during mapping of discontinuities from physical to natural space [44], requirement of different enrichment functions to tackle different material problems [45], numerical solution is sensitive to integration scheme used for enriched elements [46], and the use of blending elements for connecting the enriched elements to standard elements makes its implementation complex [47].

Extended Isogeometric Analysis (XIGA) is the other recently developed computational technique to analyse the moving discontinuities. XIGA is the extension of IGA which has been proposed as a tool to bridge the gap between design and analysis by using the non-uniform rational B-splines [48–49]. In IGA, the basis functions that are used to define the geometry of the domain are also used for the analysis part. This saves time that goes into defining the mesh and prevents geometric errors in the analysis. Further, XIGA has been extended for crack growth analysis of isotropic and orthogonal materials [50–51] and cortical bone fracture modelling [52]. However, it also requires different enrichment functions to model different material problems similar to XFEM.

Another approach proposed by Hansbo and Hansbo [53] models the discontinuities within an element with the use of additional nodal degree of freedoms (dof) present at the standard nodes. This concept is further extended into the Phantom Node Method (PNM) by Song and coworkers [54]. In this method, when an element is cut by a discontinuity, extra nodes are superposed with the original standard nodes and two superposing sub-elements are formed. This method avoids the mixed terms of stiffness K^{ua} and K^{au} at the interface of enriched and non-enriched elements and leads to a better-conditioned system matrix. However, the phantom node method is equivalent to the step-enriched XFEM [54] for modelling the strong discontinuities. Due to this similarity, the error associated with XFEM also occurs in PNM when mapping the discontinuity from physical to natural space.

Recently, the floating node method is proposed based on the development of PNM, which has a similar computational architecture to PNM, but the locations of additional nodes do not need to be fixed. These additional nodes are called floating nodes that move to the crack-edge intersections to form the crack by partitioning the original element into sub-elements. The complex crack networks can be modelled in an element by forming sub-elements that are conformal to the cracks. So far, FNM has been extended for numerous fracture problems, ranging from single crack to multiple crack problems on isotropic [55] and composite materials [13,56]. The FNM alleviates the limitations such as remeshing during crack propagation, enrichment functions requirement, error during mapping the discontinuity from physical to natural space etc. Despite its success in fracture problems, there exists some limitations during integration where during mapping a basic requirement is that the element has to be convex and severe distortion is not acceptable so that a one-to-one coordinates correspondence between physical and natural space associated with element can be guaranteed. More precisely, no interior angle should be greater than 180° for a 2D four-node element and the positivity of the Jacobian determinant should be ensured in numerical implementation [57], which increases the computational cost. Moreover, the modelling of an arbitrary crack in FNM is cumbersome as in FNM a crack divides the intact element into sub-elements. Sometimes these sub-elements may have poor aspect ratio depending on the crack direction, which deteriorates the convergence rate during the simulations. To alleviate this issue, Kumar et al. [14] considered one additional floating node in each standard element to maintain the aspect ratio of the sub-elements within the acceptable limit. To overcome these issues of integration, Liu et al. [58] proposed a smoothed finite element method by combining the FEM with strain smoothing technique of meshfree methods. In this approach, smoothing operations are performed over the elements, which eliminates the requirement of Jacobian determinant during numerical integration. The strain smoothing concept is further extended with FEM [59] and XFEM [60–61] for solving fracture problems. Though, by combining the smoothing procedures with FEM and XFEM, the requirement of mapping and positive Jacobian determinant during numerical integration is eliminated, the methods still suffer with the limitations associated with their basic framework, discussed in respective sections.

To overcome the limitations associated with FEM, XFEM, XIGA, PNM, FNM, a new approach called as Smoothed Floating Node Method (SFNM) is proposed by combining the FNM with strain smoothing technique. In SFNM, FNM is used to represent the kinematics of crack, and the system stiffness matrix is calculated by using the strain smoothing technique over the domain of the smoothing cell associated with the element. The values of stress intensity factor (SIF) are obtained from the SFNM solution using domain based interaction integral approach. The major features of the proposed method are as follows:

- No requirement of remeshing and enrichment functions to model the static and crack propagation behaviour.
- Insensitivity to the element distortion due to the absence of isoparametric mapping.
- Unlike XFEM, no mixed terms of stiffness occur, that results in better conditioning.
- Simplify integration by transforming domain integration on Gauss points into line integration along the edges.
- Shape function derivatives are not required for the field variable gradient matrix.
- Element convexity restriction is less sensitive to the computational procedure, and maintaining the aspect ratio of the sub-divided elements in SFNM becomes redundant.

To demonstrate the effectiveness of the proposed approach, three benchmark fracture mechanics problems are solved, and the results obtained by SFNM are compared with the available literature/theoretical results. In the first problem, an edge cracked plate under mode-I loading is considered and the relative error in SIF and strain energy are obtained. The second problem deals with an edge cracked plate under mode-II loading condition. The error in SIF and strain energy are obtained and compared. In the third problem, a bi-material specimen having interfacial edge crack subjected to mode-I loading is solved. The paper is organized as follows: Section 2 describes the governing equations and mathematical formulation of SFNM and smoothing technique. Section 3 and Section 4 contain the SIF computation and crack growth criterion respectively. The numerical problems are presented in Section 5 to demonstrate the effectiveness of the SFNM framework. Finally, the conclusions are drawn in Section 6.

2. Numerical formulation

In this section, the governing equations for the static analysis of an elastic medium containing a traction-free crack are briefly discussed. A brief review of FNM and SFEM is also presented for completeness. Further, the shape function generation, numerical integration procedure in SFNM and its implementation procedure is discussed.

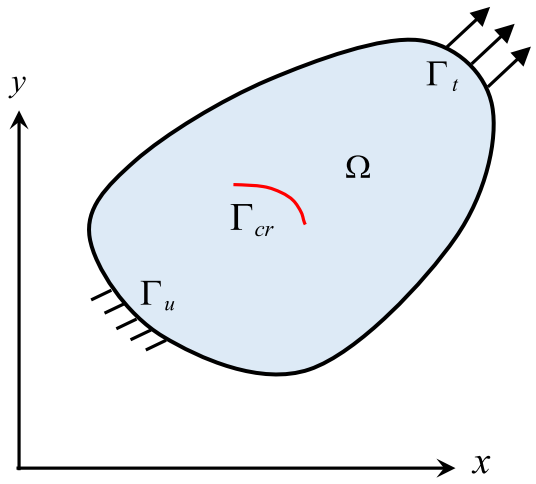

Fig. 1. A cracked domain with boundary conditions.

2.1. Governing equations for elasto-statics

Consider a linear elastic body with a discontinuity as shown in Fig. 1. The domain Ω is divided into three parts Γ_u where the displacement boundary conditions are applied, Γ_t where the traction boundary conditions are applied and Γ_{cr} which is the traction-free surface representing the discontinuity. The strong form of the static equilibrium equation along with the boundary conditions are given as,

$$\nabla.\boldsymbol{\sigma} + \mathbf{b} = 0 \text{ in } \Omega \tag{1}$$

$$\boldsymbol{\sigma}.\hat{\mathbf{n}} = \bar{\mathbf{t}} \text{ on } \Gamma_t \tag{2a}$$

$$\boldsymbol{\sigma}.\hat{\mathbf{n}} = 0 \text{ on } \Gamma_{cr} \tag{2b}$$

$$\mathbf{u} = \bar{\mathbf{u}} \text{ on } \Gamma_u \tag{2c}$$

where ∇ is the gradient operator, σ is the Cauchy stress tensor, **b** is the body force vector per unit volume, $\hat{\mathbf{n}}$ is the unit outward normal and $\bar{\mathbf{t}}$ is the applied traction vector. For small strains and displacements, the strain-displacement relation can be written as,

$$\boldsymbol{\varepsilon} = \boldsymbol{\varepsilon}(\mathbf{u}) = \nabla^s \mathbf{u} \tag{3}$$

where ∇^s is the symmetric part of the gradient operator. The constitutive relation for linear elastic material is given by Hooke's law,

$$\boldsymbol{\sigma} = \mathbf{D}\boldsymbol{\varepsilon} \tag{4}$$

where **D** is the material elasticity tensor.

By substituting the constitutive relation and the strain-displacement relation, the weak form of the equilibrium equation can be expressed as,

$$\int_{\Omega} \boldsymbol{\sigma}(\mathbf{u}) : \boldsymbol{\varepsilon}(\mathbf{v}) d\Omega = \int_{\Omega} \mathbf{b}.\mathbf{v}\, d\Gamma + \int_{\Gamma_t} \bar{\mathbf{t}}.\mathbf{v}\, d\Gamma \tag{5}$$

where **u** and **v** are the displacement trial and the test functions, respectively. Upon discretization of **u** and **v**, the above weak form can be transformed into the following discrete set of equations,

$$\mathbf{K}\mathbf{d} = \mathbf{f} \tag{6}$$

where **K** is the global stiffness matrix, **d** is the nodal displacements vector and **f** is the externally applied force vector.

2.2. Basic formulation of FNM

In FNM, each real node is characterized by its nodal coordinates and its associated dofs, and each element in the domain also contains a suitable number of floating dofs. Thus, discretized mesh contains of either intact element, or elements that encompasses a crack/discontinuity. The floating nodes in the intact element are dormant and the element is thus identical to the standard finite element. Once a crack

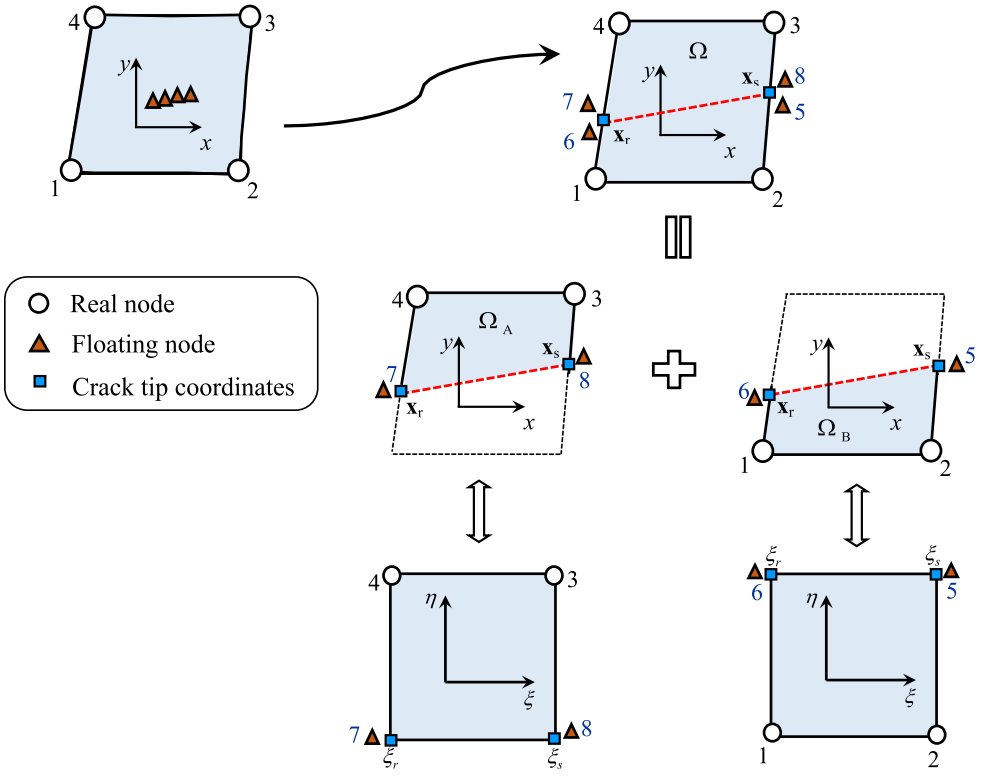

Fig. 2. A schematic representation of strong discontinuity modelling in an element using floating node method.

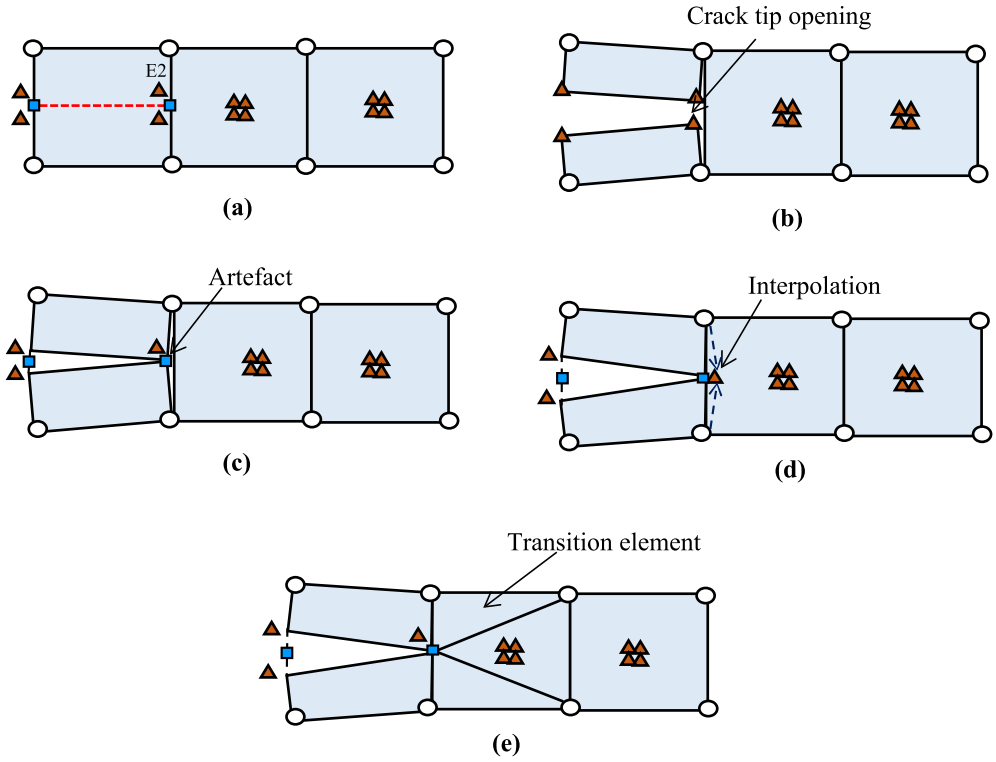

Fig. 3. Crack tip modelling in floating node method.

appears inside the intact element, the floating nodes get activated to model the crack in the element. The nodal position vectors of the floating nodes are defined by the crack position coordinates (points with coordinates $\mathbf{x}_r$ and $\mathbf{x}_s$), refer Fig. 2. Hence, the cracked element is split into two sub-elements Ω_A and Ω_B, depending on the direction of the crack [62]. The vectors of nodal coordinates of sub-elements are defined as,

$$\mathbf{x}_{\Omega_A}^T = \left[\mathbf{x}_r^T, \mathbf{x}_s^T, \mathbf{x}_3^T, \mathbf{x}_4^T\right] \quad \text{and} \quad \mathbf{x}_{\Omega_B}^T = \left[\mathbf{x}_1^T, \mathbf{x}_2^T, \mathbf{x}_s^T, \mathbf{x}_r^T\right] \tag{7}$$

Now, each sub-element ($\Omega_A$and Ω_B) has a separate Jacobian given as,

$$\mathbf{J}_A = \frac{d\mathbf{x}}{d\xi} = \frac{d\mathbf{N}}{d\xi}\mathbf{x}_{\Omega_A} \quad \text{and} \quad \mathbf{J}_B = \frac{d\mathbf{x}}{d\xi} = \frac{d\mathbf{N}}{d\xi}\mathbf{x}_{\Omega_B} \tag{8}$$

The displacement $\boldsymbol{u}_A$ and $\boldsymbol{u}_B$ in the sub-elements are interpolated separately from the respective degrees of freedom $\mathbf{d}_A$ and $\mathbf{d}_B$ of the sub-element Ω_A and Ω_B respectively,

$$\mathbf{u}_A = \mathbf{N}\mathbf{d}_A \quad \text{and} \quad \mathbf{u}_B = \mathbf{N}\mathbf{d}_B \tag{9}$$

where $\mathbf{d}_A^T = \left[\mathbf{d}_7^T, \mathbf{d}_8^T, \mathbf{d}_3^T, \mathbf{d}_4^T\right]$ and $\mathbf{d}_B^T = \left[\mathbf{d}_1^T, \mathbf{d}_2^T, \mathbf{d}_5^T, \mathbf{d}_6^T\right]$

The stiffness matrices and force vectors of the sub-elements are thus defined as,

$$\mathbf{K}_A = \int_{\Omega_A} \mathbf{B}_A^T \mathbf{D}\mathbf{B}_A \det(\mathbf{J}_A) d\Omega \quad \text{and} \quad \mathbf{K}_B = \int_{\Omega_B} \mathbf{B}_B^T \mathbf{D}\mathbf{B}_B \det(\mathbf{J}_B) d\Omega \tag{10}$$

$$\mathbf{f}_A = \int_{\Omega_A} \mathbf{N}^T \mathbf{b} \det(\mathbf{J}_A) d\Omega + \int_{\Gamma_t \cap \Gamma_{\Omega_A}} \mathbf{N}^T \bar{\mathbf{t}} \det(\mathbf{J}_A) d\Gamma \tag{11a}$$

$$\mathbf{f}_B = \int_{\Omega_B} \mathbf{N}^T \mathbf{b} \det(\mathbf{J}_B) d\Omega + \int_{\Gamma_t \cap \Gamma_{\Omega_B}} \mathbf{N}^T \bar{\mathbf{t}} \det(\mathbf{J}_B) d\Gamma \tag{11b}$$

The equilibrium equations for both sub-elements are written as,

$$\mathbf{K}_A \mathbf{d}_A = \mathbf{f}_A \quad \text{and} \quad \mathbf{K}_B \mathbf{d}_B = \mathbf{f}_B \tag{12}$$

Finally, the equilibrium equation of the floating node element is the assembly of the two sub-elements, and given as,

$$\mathbf{K}\mathbf{d} = \mathbf{f} \tag{13}$$

where $\mathbf{K} = \begin{bmatrix} \mathbf{K}_A \\ \mathbf{K}_B \end{bmatrix}$, $\mathbf{d}^T = \left[\mathbf{d}_A^T, \mathbf{d}_B^T\right]$ and $\mathbf{f}^T = \left[\mathbf{f}_A^T, \mathbf{f}_B^T\right]$ when the two sub-elements are fully separated.

The crack tip modelling in FNM is a very important aspect for failure analysis of a structure. In FNM, each individual element has the floating nodes either dormant or activated. The crack is modelled by splitting the intact element into two sub-elements by activating the floating nodes, and positioning them to the points obtained from the intersection of crack with the element edge. The split element has two floating nodes at the edge E2 of the intact element, where the crack terminates, refer Fig. 3(a). Therefore, the crack tip remains open at the edge E2 as shown in Fig. 3(b). Though the crack tip can be modelled by considering two sets of dofs from both floating nodes at the crack tip to be identical, this procedure may lead to an artefact at the crack tip as shown in Fig. 3(c), i. e. the split elements at the crack tip do not have adequate topology for connecting with the adjacent intact element, resulting in a lack of displacement compatibility at the element edge E2. To alleviate this issue, the dofs at the crack tip are interpolated from the neighbouring dofs as illustrated in Fig. 3(d). Hence, the intact element adjacent to the crack tip is considered as a transition element (refer Fig. 3(e)) to maintain the displacement compatibility between the split element and intact element. The detailed procedure can be found in the literature [14]. The transition element is considered at the crack tip which is further divided into triangular elements to improve the accuracy of the results.

2.3. Strain smoothing technique

The strain smoothing was first introduced by Chen et al. [63] for meshfree methods, and later extended in the framework of FEM [59,64–67]. The strain smoothing technique can achieve higher accuracy and convergence rates than the standard finite element method,

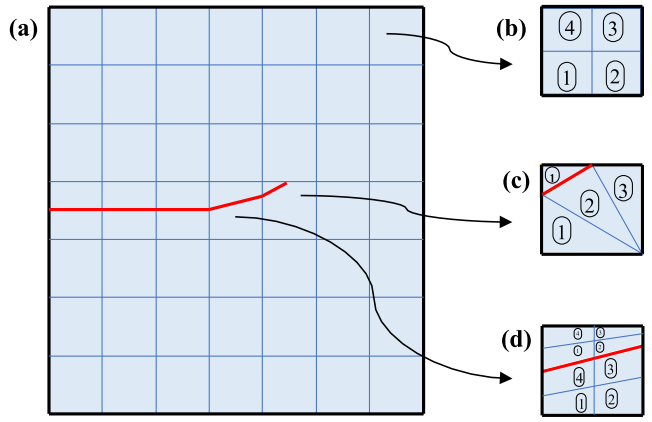

Fig. 4. Schematic of subcells formation for integration in SFNM: **(a)** crack growth in domain **(b)** intact element subcells **(c)** 2 sub-elements with inclined crack path and further subdivision into triangular subcells and **(d)** 2 quadrilateral sub-elements with inclined crack path and further subdivision into quadrilateral subcells.

especially in the presence of singularities or distorted meshes, for a slightly smaller computational cost. In the meshfree method based on nodal integration form, the integration in **Eq. (5)** is performed over representative cells of nodes in the problem domain. To guarantee the convergence of the solution, the linear exactness in the solution of the weak form should be ensured. To meet this requisite, the following integration constraint should be satisfied [63,68],

$$\int_{\Omega} \mathbf{B}_I^T(\mathbf{x}) d\Omega = \int_{\Gamma_t} \mathbf{N}_I^T(\mathbf{x}) d\Gamma \tag{14}$$

with

$$\mathbf{B}_I = \begin{bmatrix} N_{I,1} & 0 \\ 0 & N_{I,2} \\ N_{I,2} & N_{I,1} \end{bmatrix}, \quad \mathbf{N}_I = \begin{bmatrix} N_I n_1 & 0 \\ 0 & N_I n_2 \\ N_I n_2 & N_I n_1 \end{bmatrix} \tag{15}$$

where $\mathbf{B}_I$ is the standard gradient matrix of node I, N_I is the shape function of node I, n_1 and n_2 are the first and second components of the outward boundary normal vector of the smoothing cell. This condition is met by applying strain smoothing techniques for each representative nodal cell.

Table 1
Shape function value at different sites within SC4Q4 element (Fig. 6 **(d)**).

Site	Node 1	Node 2	Node 3	Node 4	Description
1	1	0	0	0	Field node
2	0	1	0	0	Field node
3	0	0	1	0	Field node
4	0	0	0	1	Field node
5	0.5	0.5	0	0	Edge midpoint
6	0	0.5	0.5	0	Edge midpoint
7	0	0	0.5	0.5	Edge midpoint
8	0.5	0	0	0.5	Edge midpoint
9	0.25	0.25	0.25	0.25	Intersection of two bi-medians

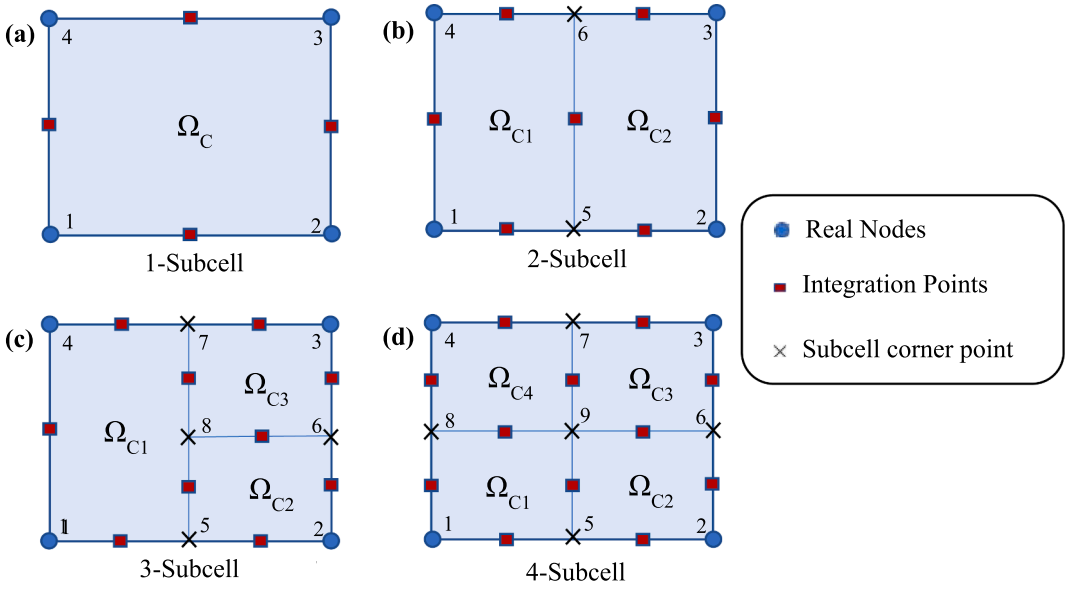

Fig. 5. Quadratic element division into smoothing subcells and integration scheme: **(a)** 1-subcell **(b)** 2-subcells **(c)** 3-subcells and **(d)** 4-subcells.

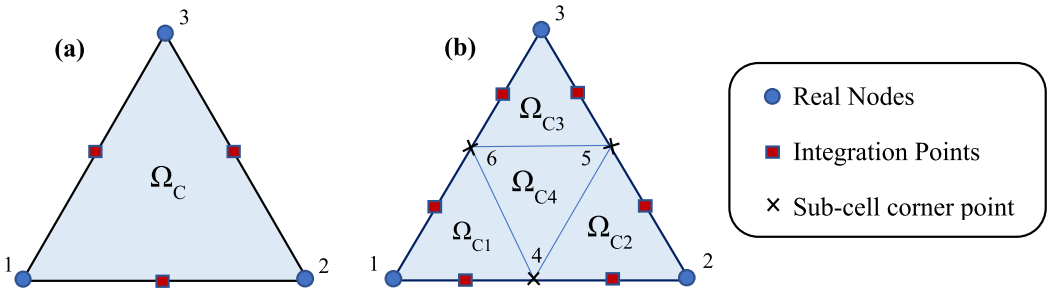

Fig. 6. Triangular element division into smoothing subcells and integration scheme: **(a)** 1-subcell **(b)** 4-subcells.

Table 2
Shape function values at different sites within SC1T3 element (Fig. 7(b)).

Site	Node 1	Node 2	Node 3	Description
1	1	0	0	Field node
2	0	1	0	Field node
3	0	0	1	Field node
4	0.5	0.5	0	Edge midpoint
5	0	0.5	0.5	Edge midpoint
6	0.5	0	0.5	Edge midpoint

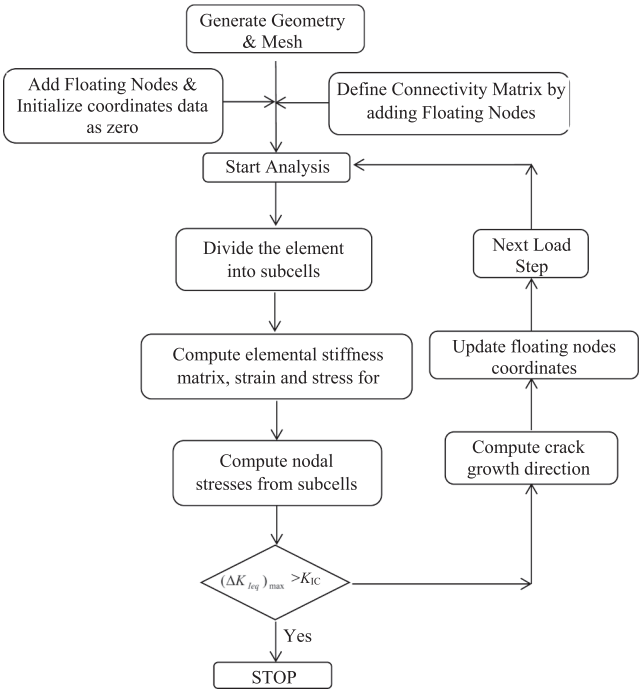

Fig. 7. Detailed procedure in SFNM for modelling crack initiation to final failure.

The motivation of this work is to develop a Smoothed FNM by incorporating the strain smoothing technique in the framework of FNM. In SFNM, sub-elements are formed as in the FNM, but they are further subdivided into several smoothing subcells (see Fig. 4) and integrated using the smoothing technique to elevate distortion sensitivity. When choosing a constant smoothing function, area integration over the sub-cell becomes line integration along its boundaries, and no gradient of shape functions is required in computing the field gradients or in forming the stiffness matrix. The integration along the edges of each subcell is done numerically using 1D Gauss integration scheme. Fig. 5 shows the field nodes and integration points corresponding to different number of subcells. A smoothing operation is performed to the gradient of displacement for all the subcells in an element. Let u represent the displacement along a certain direction, the smoothing operation for its gradient at a point $\mathbf{x}_c$ (belonging to a subcell domain Ω_C) is given as,

$$\tilde{\nabla} u(\mathbf{x}_c) = \int_{\Omega} \nabla u(\mathbf{x}) \phi(\mathbf{x} - \mathbf{x}_c) d\Omega \tag{16}$$

Using Integration by parts, the right-hand side of **Eq. (16)** becomes,

$$\tilde{\nabla}\ u(\mathbf{x}_c) = \int_{\Gamma} u(\mathbf{x}) \mathbf{n}(\mathbf{x}) \phi(\mathbf{x} - \mathbf{x}_c) d\Gamma - \int_{\Omega} u(\mathbf{x}) \nabla \phi(\mathbf{x} - \mathbf{x}_c) d\Omega \tag{17}$$

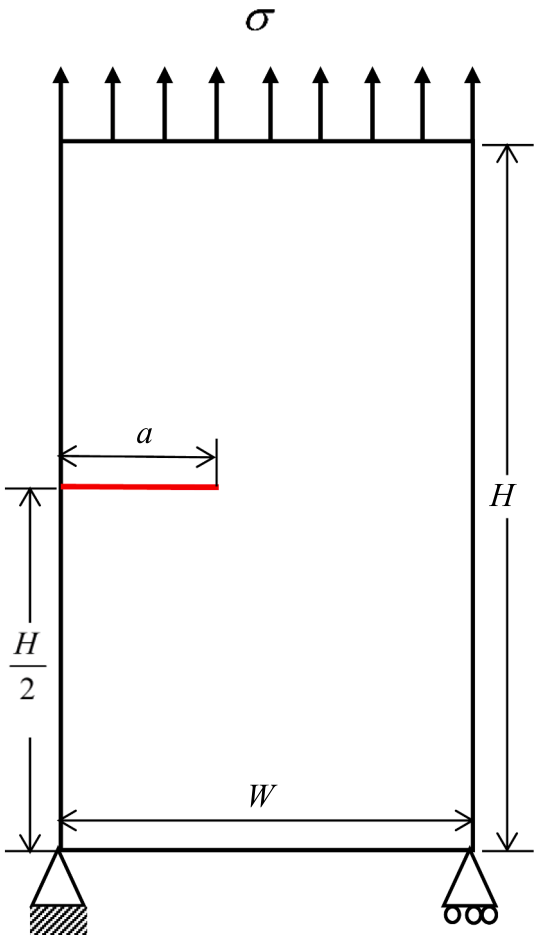

Fig. 8. A rectangular plate with an edge crack under mode-I loading.

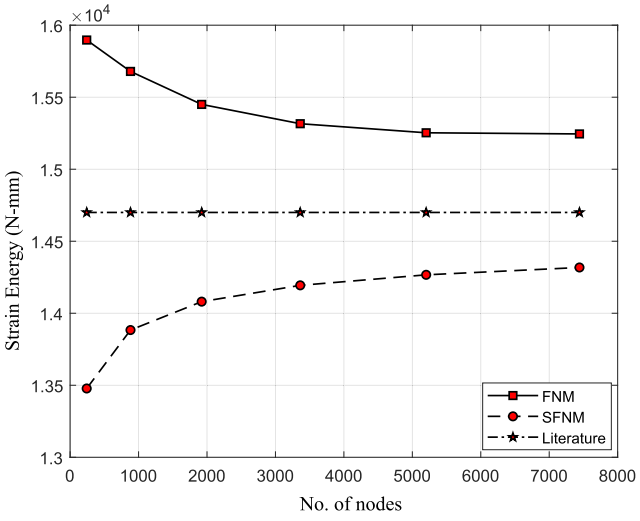

Fig. 9. The convergence in strain energy for the rectangular plate with edge crack under mode-I loading.

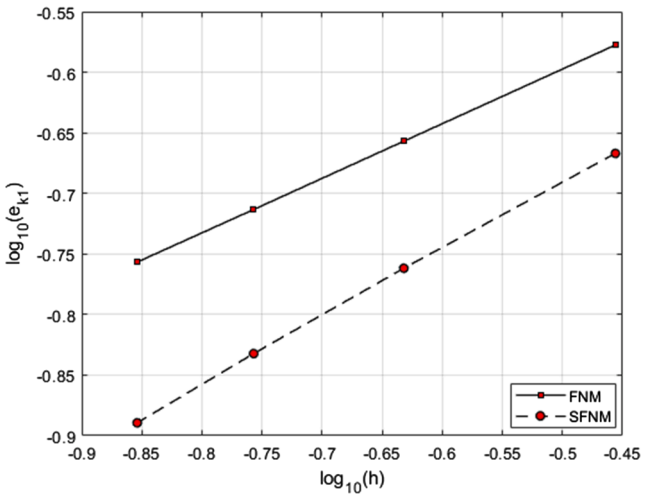

Fig. 10. Comparison of convergence rate between FNM and SFNM in the SIF.

where ϕ is a smoothing function. A piecewise constant smoothing function is considered here, which is constant within Ω_C and vanish everywhere else,

$$\phi(\mathbf{x}-\mathbf{x}_c)=\begin{cases}1/A_C & \boldsymbol{x}\in\Omega_C\\ 0 & \boldsymbol{x}\notin\Omega_C\end{cases} \tag{18}$$

$$A_C=\int_{\Omega_C} d\Omega$$

The second term of the right hand side of **Eq. (17)** vanishes with the chosen ϕ. Substituting ϕ into **Eq. (17)**, we get the smoothed gradient of displacement as,

$$\widetilde{\nabla}u(\mathbf{x}_c)=\int_{\Gamma_C}u(\mathbf{x})\mathbf{n}(\mathbf{x})\phi(\mathbf{x}-\mathbf{x}_c)d\Gamma=\frac{1}{A_C}\int_{\Gamma_C}u(\mathbf{x})\mathbf{n}(\mathbf{x})d\Gamma \tag{19}$$

where Γ_C is the boundary of the smoothing subcell. Here, the choice of piece-wise constant smoothing function ϕ converts the area integration (**Eq. (16)**) into line integration along the edges of the subcell. The smoothed displacement gradient becomes independent of $\mathbf{x}_c$, i.e., constant within Ω_C. Repeating the above procedure for the displacement vector $\mathbf{u}$ and substituting the smoothed gradients into **Eq. (3)**, the smoothed strain at $\mathbf{x}_c$ can be obtained as,

$$\widetilde{\boldsymbol{\varepsilon}}(\mathbf{x}_c)=\sum_{I=1}^{n}\mathbf{B}_I(\mathbf{x}_c)\mathbf{d}_I \tag{20}$$

where n is the number of nodes and $\mathbf{B}_I$ is the smoothed strain matrix of node I. For 2D, it is written as,

$$\widetilde{\mathbf{B}}_I(\mathbf{x}_c)=\begin{bmatrix}\widetilde{b}_{I1}(\mathbf{x}_c) & 0\\ 0 & \widetilde{b}_{I2}(\mathbf{x}_c)\\ \widetilde{b}_{I2}(\mathbf{x}_c) & \widetilde{b}_{I1}(\mathbf{x}_c)\end{bmatrix} \tag{21}$$

where

$$\widetilde{b}_{Ik}(\mathbf{x}_c)=\frac{1}{A_C}\int_{\Gamma_C}N_I(\mathbf{x})n_k(\mathbf{x})d\Gamma,\quad (k=1,2)$$

If one Gaussian point is used for line integration along each segment of the boundary Γ_i^C of Ω_C, the above equation can be transformed to its algebraic form as,

$$\widetilde{b}_{Ik}(\mathbf{x}_c)=\sum_{i=1}^{M}N_I\left(\mathbf{x}_i^{GP}\right)n_{ik}^C l_i^C \tag{22}$$

where M is the number of boundary segments, $\mathbf{x}_i^{GP}$ is the Gaussian point of the i^{th} boundary segment Γ_i^C, l_i^C is the length and n_i^C the outward unit normal vector of Γ_i^C, respectively. Once the smoothed gradient matrix over each subcell is evaluated, the smoothed element stiffness matrix of the sub-element e of SFNM can be obtained by assembly from all the subcells in the element as,

$$\mathbf{K}_e^{\text{SFNM}}=\sum_{\forall C\in e}\widetilde{\mathbf{B}}_C^T\mathbf{D}\widetilde{\mathbf{B}}_C A_C \tag{23}$$

where $\widetilde{\mathbf{B}}_C$ (i.e., $[\widetilde{\mathbf{B}}_I(\mathbf{x}_c),\cdots,\widetilde{\mathbf{B}}_n(\mathbf{x}_c)]$) is the smoothed gradient matrix of the subcell C. Now, the final discretized algebraic system of equation for the split elements can be written as,

$$\mathbf{K}_{\text{A}}^{\text{SFNM}}\mathbf{d}_{\text{A}}=\mathbf{f}_{\text{A}}\quad\text{and}\quad\mathbf{K}_{\text{B}}^{\text{SFNM}}\mathbf{d}_{\text{B}}=\mathbf{f}_{\text{B}} \tag{24}$$

Finally, the algebraic equation of SFNM is the assembly of the two sub-elements,

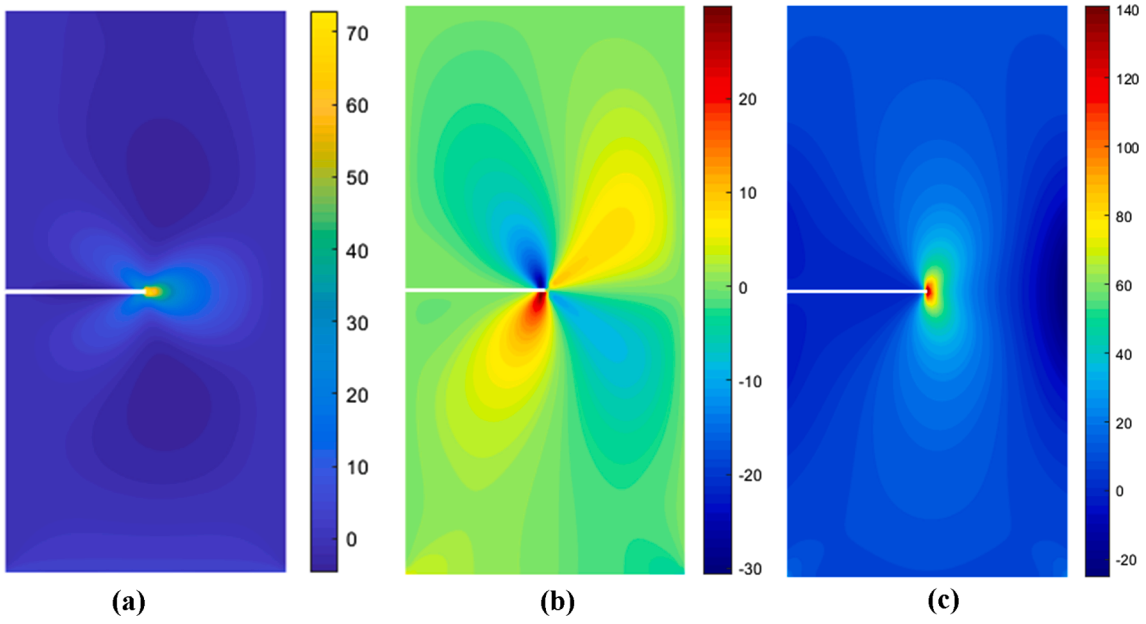

Fig. 11. Static edge crack plate stress contours under mode-I loading: **(a)** σ_{xx} **(b)** σ_{xy} **(c)** σ_{yy}.

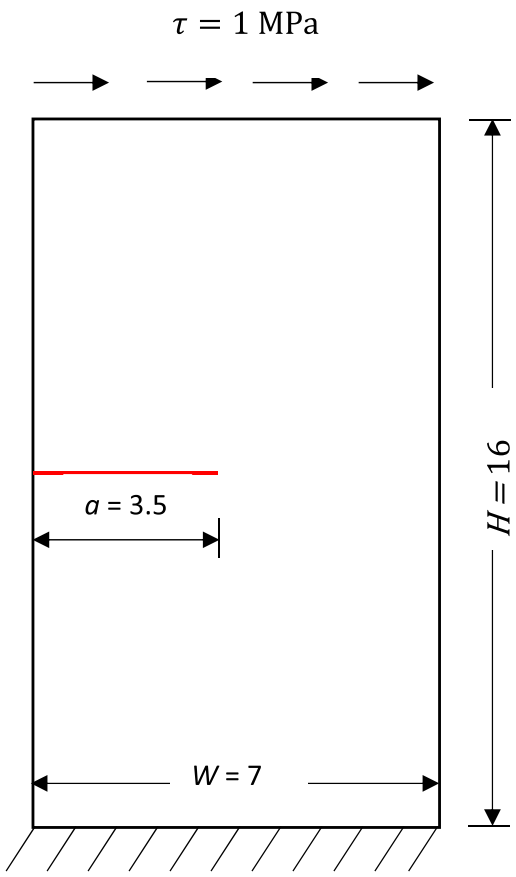

Fig. 12. A rectangular plate with an edge crack under shear (mode-II) loading, dimensions are in mm.

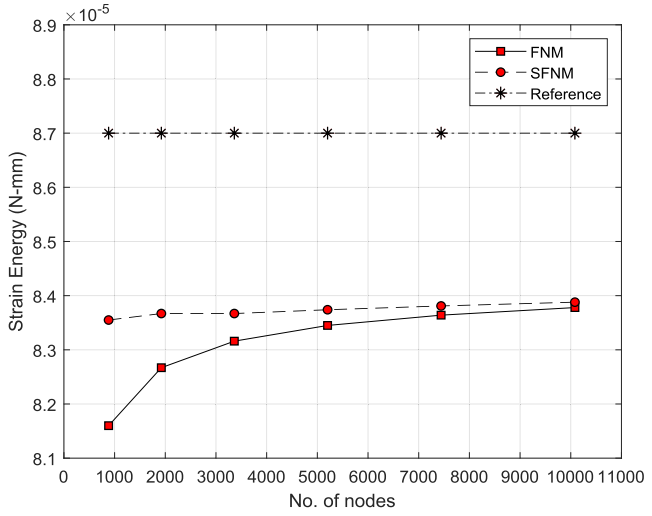

Fig. 13. The convergence in strain energy for the rectangular plate with edge crack under mode-II loading.

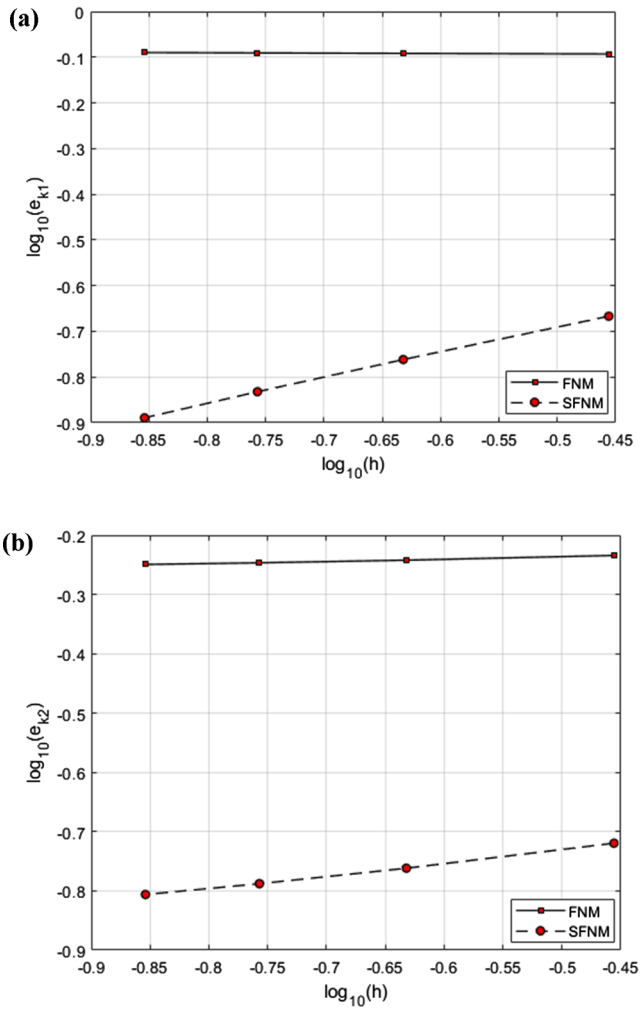

Fig. 14. Comparison of convergence rate of SIF vs mesh size (h) between FNM and SFNM; **(a)** convergence in SIF K_{I} **(b)** convergence in SIF K_{II}.

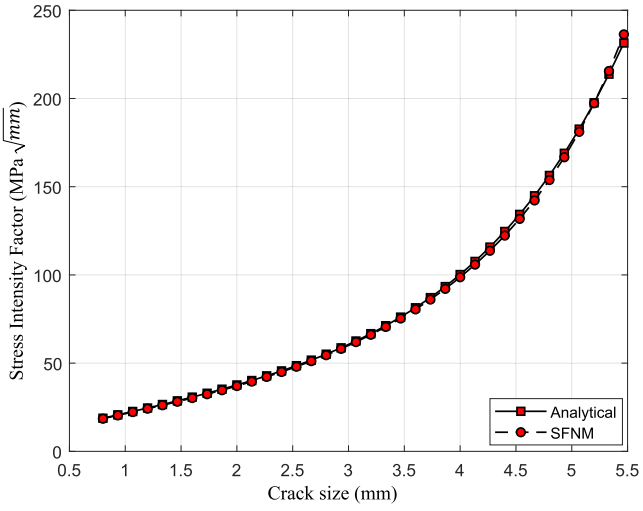

Fig. 15. SIF variation with crack length under mode-I loading for edge crack plate.

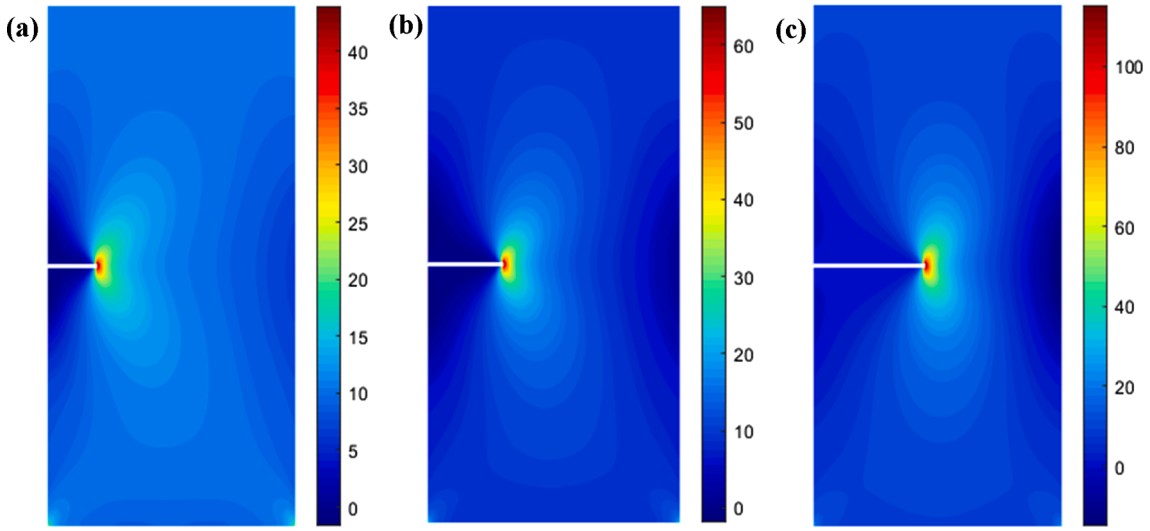

Fig. 16. Normal stress contour of edge crack plate under normal load; **(a)** $\frac{a}{W} = 0.2$, **(b)** $\frac{a}{W} = 0.3$ and **(c)** $\frac{a}{W} = 0.45$

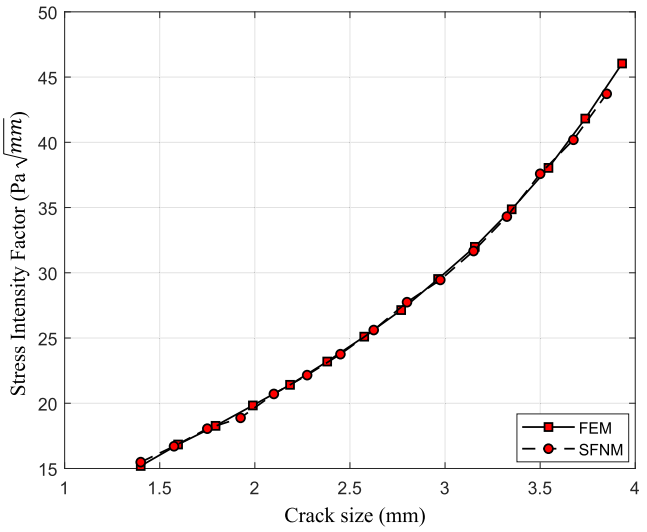

Fig. 17. SIF variation with crack length under mode-II loading for edge crack plate.

$$\mathbf{K}^{\mathrm{SFNM}}\mathbf{d} = \mathbf{f} \tag{25}$$

$$\mathbf{K}^{\mathrm{SFNM}} = \begin{bmatrix} \mathbf{K}_{\mathrm{A}}^{\mathrm{SFNM}} \\ \mathbf{K}_{\mathrm{B}}^{\mathrm{SFNM}} \end{bmatrix}$$

2.4. Shape function construction and numerical integration scheme

In this section, we focus on the construction of the shape functions and integration scheme for the elements used in SFNM. In SFNM, both 4-node quadrilateral and 3-node triangular elements are used for the numerical simulations as shown in Fig. 4. The number of subcells in an element depends on the required accuracy. In this work during smoothing procedure, 4-node quadrilateral element is divided into 4-subcells, however the procedure for dividing the quadrilateral element from 1-subcell to 4-subcells is discussed and illustrated in Fig. 5. Similarly, the 3-node triangular element is divided into 1-subcell during the simulations, but the procedure to divide it into 1-subcell and 4-subcells is illustrated in Fig. 6 for generalization. It is observed that SFEM solution using 1-subcell is equivalent to the FEM reduced integration [59]. The explicit shape functions themselves are used at the nodal points. The shape functions are interpolated simply by a linear function at any point on the boundary. For example, in Fig. 5(b) the element is divided into 2-subcells and the nodal points (1, 2, 3, 4) have the shape function values as node-1 (1, 0, 0, 0), node-2 (0, 1, 0, 0), node-3 (0, 0, 1, 0) and node-4 (0, 0, 0, 1) for a quadrilateral element. At intermediate midpoints 5 and 6, the shape functions are calculated through linear shape functions of two related nodes on the edge and obtained as (0.5, 0.5, 0, 0) and (0, 0, 0.5, 0.5) respectively. In the same manner, we can write the shape functions for the edges of 3-subcells and 4-subcells shown in Fig. 5(c) and (d) respectively. Detailing of shape function values corresponding to 4-subcells of quadrilateral (SC4Q4) element is given in Table 1.

Through the 4-node quadrilateral elements are used for meshing the problem domain, the element inside the domain may have triangular sub-elements at the split element cut by an arbitrary crack (see Fig. 4(c)) and inside the transition element (see Fig. 3). Therefore, a set of nodal shape function values for triangular element may be taken as [(1, 0, 0), (0, 1, 0), (0, 0, 1)]. Table 2 represents the shape function values of 4-smoothing subcells of triangular element (SC4T3) as shown in Fig. 6 (b). For simplicity, 1-subcell (Fig. 6(a)) of the triangular element is considered for the computational purpose in the current work.

To compute the smoothed strain-displacement gradient matrix, the shape function is required only along the boundary of the subcells. The stiffness matrix is obtained from linear integration along the boundaries of each subcell. The division of the cracked element and intact element along with subcells formation is shown in Fig. 4. A crack separates an element into two sub-elements and each sub-element further qualifies for the number of subcells for the boundary integration. In case the crack makes a partition such that intact element is divided into 1-triangle and 5-sided polygon, then that element is divided into the number of triangular subcells as shown in Fig. 4(c) and line integration is performed along each boundary of the triangular subcell. Crack touching any standard node of FE element may lead to the development of triangular as well as quadrilateral sub-elements. The smooth stiffness matrix is computed using **Eq. (23)** for the smooth domain of subcell and global stiffness is calculated with the assemblage of the elemental stiffness. In the same way, smooth strain-displacement matrix and strain are computed corresponding to each subcell by using **Eq. (21)** and **Eq. (20)** respectively.

For the comparison purpose, the conventional Gauss quadrature integration procedure is also applied with FNM, and the obtained results are compared with the SFNM results. Kumar et al. [14] discussed the integration scheme with respect to the aspect ratio for curved crack problems. A crack passing close to one of the standard nodes of the element may lead to a skewed aspect ratio. It shows the division of the

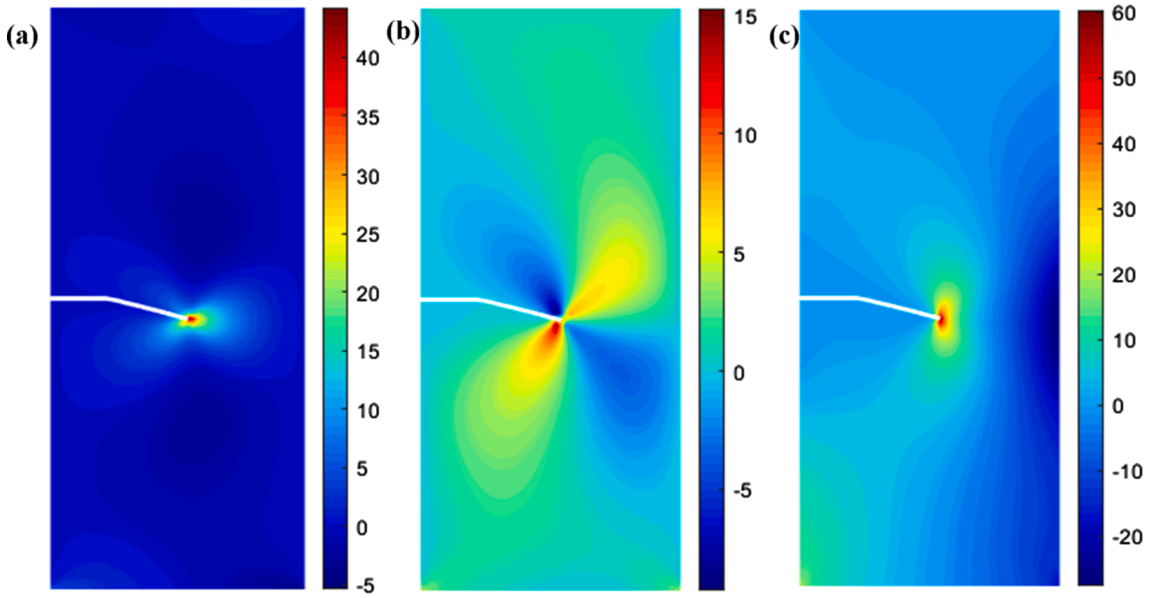

Fig. 18. Stress contour plots of edge crack plate under shear load at $\frac{a}{W} = 0.5$: **(a)** σ_{xx} **(b)** σ_{xy} **(c)** σ_{yy}

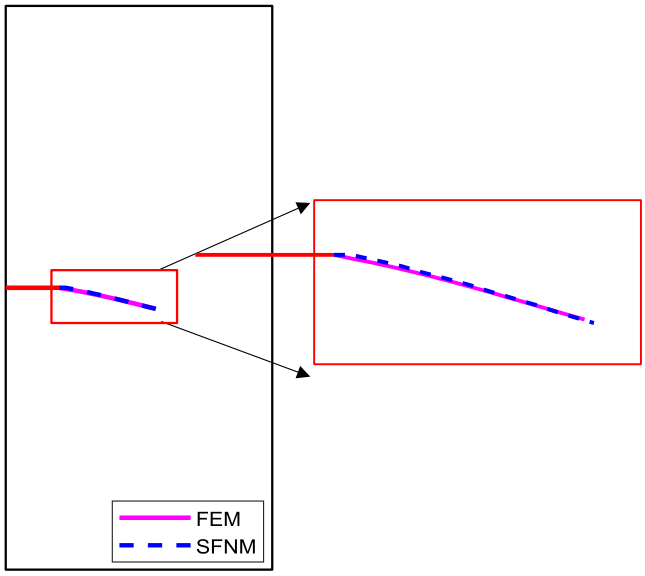

Fig. 19. Crack growth trajectory comparison of an edge crack plate under mode-II loading.

element into a triangular and pentagon sub-elements. Integration of triangular sub-element using Gauss quadrature is straightforward but the pentagon sub-element is further divided into 3 triangles in case of the element is restricted to 4 floating nodes. To compensate the poor aspect ratio, instead of 4 floating nodes, 5 floating nodes are used to maintain the appropriate aspect ratio in accordance to Gauss quadrature integration. The 5th floating node inside the domain is inserted iteratively. The procedure to insert an extra float node and creating the triangular sub-elements is available in [14]. To tackle the poor aspect ratio, inserting an extra floating node adds the complexity in the computation. This drawback may be resolved precisely by using the smoothing integration approach as shown in Fig. 5 and Fig. 6.

2.5. SFNM outline

FNM formulation is explained in section 2.2. Detailing of the division of an intact element into sub-elements due to discontinuity and the activation and positioning of the floating nodes is also demonstrated in the same section. In the continuation of this, strain-displacement matrix according to the smoothing approach is required. Displacement gradient for the calculation of smoothed domain given in **Eq. (23)** can be recalled from the **Eq. (21)**. The explicit shape functions as mentioned in Table 1 and normal unit vectors are sufficient to proceed for the line integration approach. The steps required in SFNM to model crack propagation are detailed in the flow chart given in Fig. 7.

3. SIF computation

The stress intensity factor is a critical parameter that has frequently been used in fracture mechanics problems of brittle materials. The virtual crack closure technique (VCCT) and interaction integral approach are the commonly used approach in literature for calculating the SIF values. However, the VCCT approach is cumbersome to implement in generic crack propagation problems as it generally requires uniform mesh. Therefore, in this paper, a domain-based interaction integral approach is used in conjunction with SFNM to compute the values of SIF. For two independent equilibrium states of a cracked body, the domain form of interaction integral can be written as,

$$I^{(1,2)} = \int_A \left[\boldsymbol{\sigma}_{ij}^{(1)} \frac{\partial u_i^{(2)}}{\partial x_1} + \boldsymbol{\sigma}_{ij}^{(2)} \frac{\partial u_i^{(1)}}{\partial x_1} - \mathbf{W}^{(1,2)} \delta_{1j} \right] \frac{\partial q}{\partial x_j} dA \tag{26}$$

where $\mathbf{W}^{(1,2)}$ is the interaction strain energy term associated with actual and auxiliary states, q is a smoothing weight function,$\boldsymbol{\sigma}_{ij}$ is the stress field, 1 and 2 signify the actual and auxiliary state respectively. For the bi-material interface cracked body, the interaction integral form can be written as,

$$I^{(1,2)} = \sum_{m=1}^{2} \int_{A_m} \left[\boldsymbol{\sigma}_{ij}^{(1)} \frac{\partial u_i^{(2)}}{\partial x_1} + \boldsymbol{\sigma}_{ij}^{(2)} \frac{\partial u_i^{(1)}}{\partial x_1} - \mathbf{W}^{(1,2)} \delta_{1j} \right] \frac{\partial q}{\partial x_j} dA \tag{27}$$

where m represents a particular material in the bi-material domain. In LEFM, the relationship between interaction integral and SIF is given as,

$$I^{(1,2)} = \frac{2\left(K_I^{(1)} K_I^{(2)} + K_{II}^{(1)} K_{II}^{(2)}\right)}{E^* cosh^2(\pi\epsilon)} \tag{28}$$

where

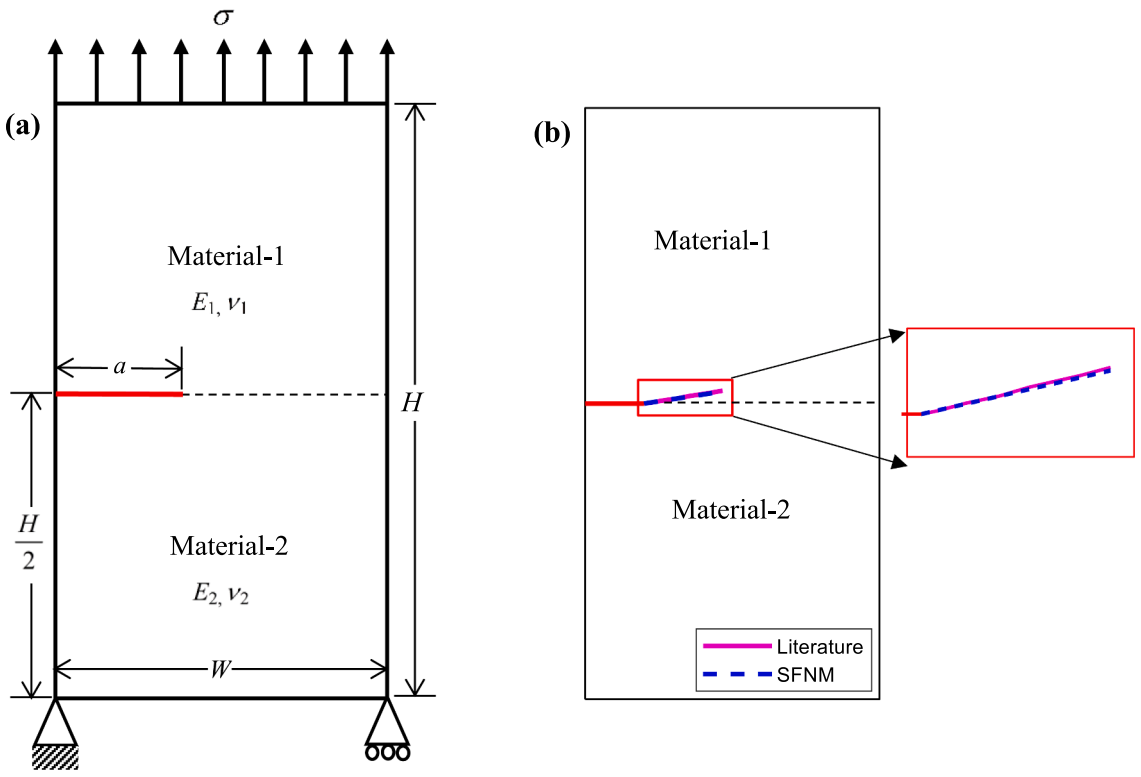

Fig. 20. **(a)** Bi-material plate with an interfacial edge crack under mode-I loading; **(b)** Crack growth trajectory comparison of a bi-material interface edge crack.

Table 3
Properties of the constituents of bi-materials rectangular plate.

	Young's Modulus, E (GPa)	Poisson's ratio, ν	Fracture toughness, K_{IC} (MPa.m$^{0.5}$)
Material-1	74	0.30	40
Material-2	200	0.30	60

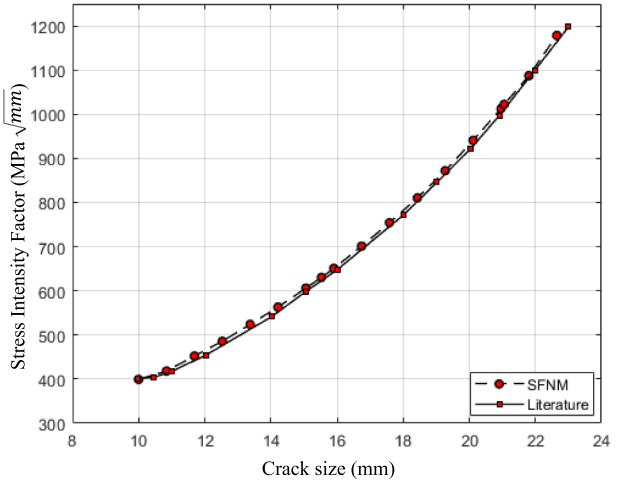

Fig. 21. SIF vs crack length plot for bi-materials edge crack plate under mode-I loading; Literature results refer [14].

$$\frac{2}{E^*} = \frac{1}{E_1} + \frac{1}{E_2}$$

For bi-material interfacial cracks, the auxiliary fields [69] can be written as,

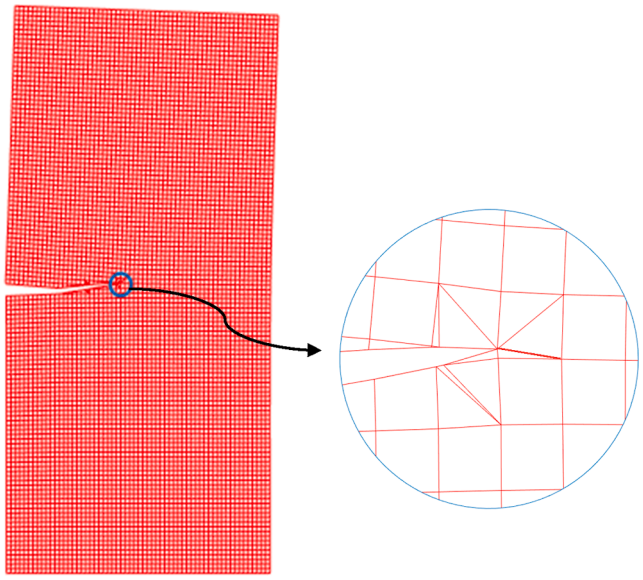

Fig. 22. Deformed configuration with element subdomains for bi-material edge crack plate under mode-I loading.

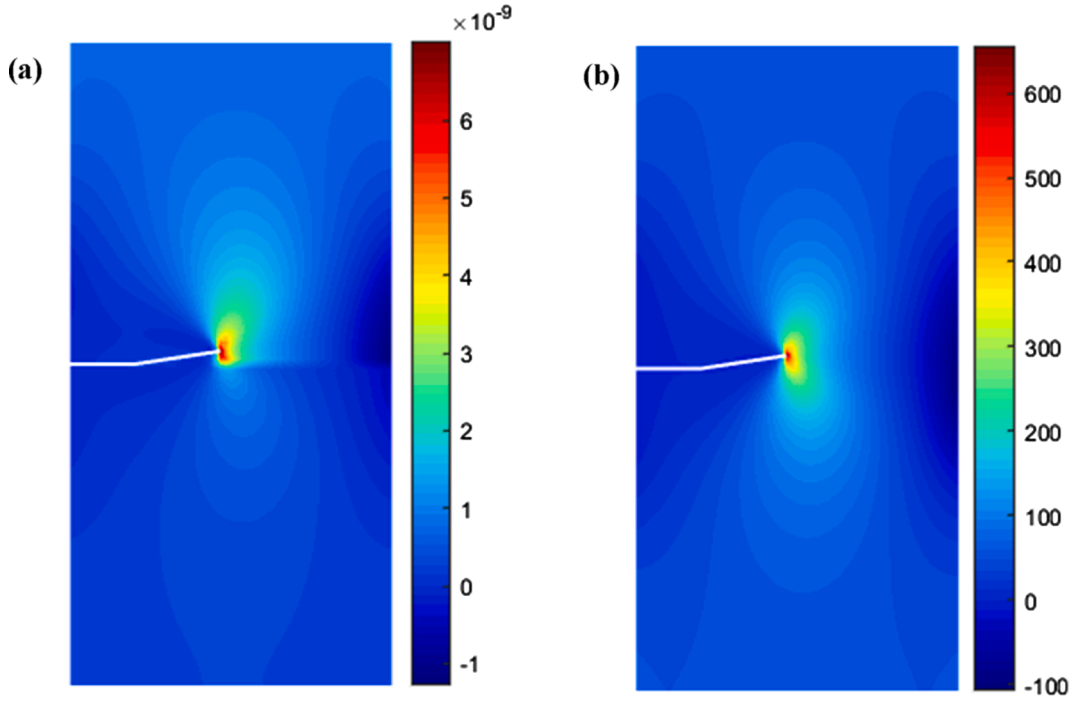

Fig. 23. Stress and Strain contour plot at failure condition; **(a)** strain contour plot in *y*-direction **(b)** stress contour plot in y-direction.

$$u_i = \begin{cases} \dfrac{1}{4\mu_1 cosh(\pi\epsilon)}\sqrt{\dfrac{r}{2\pi}} f_i(r,\theta,\epsilon,\kappa_1) & \text{for upper half plane} \\ \dfrac{1}{4\mu_2 cosh(\pi\epsilon)}\sqrt{\dfrac{r}{2\pi}} f_i(r,\theta,\epsilon,\kappa_2) & \text{for lower half plane} \end{cases} \tag{29}$$

where μ is the shear modulus, (r,θ) are the polar coordinates. The details of computing the functions f_1 and f_2 can be found in the literature [35]. The parameters ϵ and κ are bi-material constants and defined as,

$$\epsilon = \frac{1}{2\pi}\log\left(\frac{1-\overline{\beta}}{1+\overline{\beta}}\right)$$

where, $\overline{\beta}$ is the second Dundurs parameter and defined as,

$$\overline{\beta} = \frac{\mu_1(\kappa_2-1)-\mu_2(\kappa_1-1)}{\mu_1(\kappa_2+1)+\mu_2(\kappa_1-1)}$$

and

$$\kappa_i = \begin{cases} 3-4\upsilon_i & \text{plane strain} \\ \dfrac{3-\upsilon_i}{1+\upsilon_i} & \text{plane stress} \end{cases}$$

where υ is Poisson's ratio.

The mixed-mode SIF values can be obtained from **Eq. (28)** using $K_I^{(2)} = 1$ and $K_{II}^{(2)} = 0$ and vice versa.

$$K_I = \frac{E^* cosh^2(\pi\epsilon)}{2} I^{(1)} \tag{30a}$$

$$K_{II} = \frac{E^* cosh^2(\pi\epsilon)}{2} I^{(2)} \tag{30b}$$

4. Crack propagation criterion

To determine the crack growth direction, a particular requisite criterion needs to be prescribed. Due to the cyclic loading, the crack may reach to the critical length which causes severe fracture failure of the structural components. To avoid the fracture failure, crack growth rate and propagation direction are predicted. The discrete set of equations are solved to obtain the displacements, and the stress intensity factor values are extracted from **Eq. (30)**. The range of SIF for both mode-I and mode-II under constant amplitude cyclic loading is defined as,

$$\Delta K = K_{max} - K_{min} \tag{31}$$

where $K_{\max}$ and $K_{\min}$ are the SIF values corresponding to maximum and minimum applied loads respectively. In this study, the maximum circumferential stress criterion is employed to obtain the direction of crack growth. The equivalent SIF and the direction of crack growth θ_c, at each crack increment are obtained using the following expressions,

$$\Delta K_{Ieq} = \Delta K_I cos^3\left(\frac{\theta_c}{2}\right) - 3\Delta K_{II} cos^2\left(\frac{\theta_c}{2}\right) sin\left(\frac{\theta_c}{2}\right) \tag{32}$$

$$\theta_c = 2\arctan\frac{1}{4}\left\{\frac{K_I}{K_{II}} \pm sign(K_{II})\sqrt{\left(\frac{K_I}{K_{II}}\right)^2 + 8}\right\} \tag{33}$$

Failure takes place whenever $(\Delta K_{Ieq})_{max} > K_{IC}$, where $(\Delta K_{Ieq})_{max}$ is the equivalent stress intensity factor corresponding to maximum load and K_{IC} is the fracture toughness of the material.

5. Numerical examples

In this section to illustrate the accuracy and effectiveness of the proposed SFNM, both static and crack propagation examples are considered for simulations and the results obtained by SFNM are compared with the FNM and available literature results. All the simulations are performed under plane strain condition. In all the problems, a uniform initial mesh of quadrilateral elements is used in the entire domain. The LEFM theory is considered in the simulations, where the crack tip is singular at the crack tip. Thus, special crack tip elements are required to model the crack tip singularity. However, in the present work, an special transition element within the SFNM framework is used just ahead of the crack tip (see Fig. 3e), which improves the accuracy of the results. Moreover, the values of SIF are obtained using the domain-based interaction integral approach, which considers the global quantities far from the crack tip for SIF computation and reduces the effect of singularity on the numerical results.

5.1. Static crack examples

In this section, the accuracy and convergence properties of the proposed SFNM are numerically studied within the LEFM framework in 2D static crack problems under mode-I and mode-II loading conditions. The numerical results from the proposed SFNM formulation are compared with the FNM and literature results. The strain energy and error in SIF are used to estimate the error and convergence properties of the proposed SFNM.

5.1.1. Plate with an edge crack under mode-I loading

In this example, a rectangular plate with an edge crack is analysed under tension loading ($\sigma = 10$ MPa). The basic geometry along with the dimensions ($a = 4$ mm, $H = 16$ mm, $W = 8$ mm) and boundary conditions are shown in Fig. 8. The thickness of the plate is taken as 1 mm. The material properties are taken from Ref. [67]. They are given as: Young's modulus $E = 1$ MPa, Poisson's ratio $\nu = 0.3$. The strain energy and the error in the SIF are given as,

$$E_{(\Omega)} = \frac{1}{2}\int_{\Omega} \boldsymbol{\varepsilon}^{\mathbf{T}}\ \mathbf{D}\ \boldsymbol{\varepsilon}\ d\Omega \tag{34}$$

$$e_k = \left|\frac{K_{SIF}^{num} - K_{SIF}^{ref}}{K_{SIF}^{ref}}\right|^{1/2} \times 100\%, \quad \text{SIF} = I, II \tag{35}$$

where the superscript "*ref*" denotes the reference solution and "*num*" denotes the numerical solution.

For the simulation purpose, the domain is discretized by a structured mesh with 4-node quadrilateral (Q4) elements for both FNM and SFNM. Different mesh sizes i.e. 242 nodes (11 × 22), 882 nodes (21 × 42), 1922 nodes (31 × 62), 3362 nodes (41 × 82), 5202 nodes (51 × 102) and 7442 nodes (61 × 122) are considered for checking convergence properties of the proposed approach. The strain energy and relative error in SIF values are computed and plotted with respect to mesh size, then SFNM results are compared with the FNM and literature results. Fig. 9 shows the comparison of strain energy values obtained through SFNM and FNM with the literature in mode-I loading. From the figure, it is apparent that the convergence of SFNM is slightly better than FNM. Further, the relative error in SIF values is plotted with the mesh size in log scale for SFNM and FNM as shown in Fig. 10. From the comparison, it is evident that the SFNM technique is more accurate and gives better convergence rate than the FNM. The SIF relative error using SFNM is significantly less in comparison to SIF relative error using FNM as shown in Fig. 10. The **s**tress contours are also plotted for illustration purpose in Fig. 11.

5.1.2. Plate with an edge crack under shear

Next, to illustrate the ability of the SFNM, we consider a rectangular plate with an edge crack subjected to pure shear traction on the top surface as shown in Fig. 12. The bottom of the plate is fixed and plane strain condition is assumed for simulation. The geometry parameters used in the computation are: width $W = 7$ mm, height $H = 16$ mm, crack length $a = 3.5$ mm. The material properties; Young's modulus E and Poisson's ratio ν are taken as 3×10^7 Pa and 0.25 respectively. The reference values of SIFs for this case are taken from the literature [71] and given as $K_I = 34Pa\sqrt{mm}$, $K_{II} = 4.55Pa\sqrt{mm}$. Different mesh sizes i. e. 882 nodes (21 × 42), 1922 nodes (31 × 62), 3362 nodes (41 × 82), 5202 nodes (51 × 102), 7442 nodes (61 × 122) and 10,082 nodes (71 × 142) are considered to analyse the convergence properties of the proposed framework. The strain energy convergence with respect to mesh refinement is shown in Fig. 13, which depicts that the strain energy convergence is better in SFNM than in FNM. In addition, the mesh convergences of stress intensity factors K_{I} and K_{II} are presented in Fig. 14 (a) and Fig. 14(b) respectively. In both cases, it is evident that a significant reduction of error is achieved in SFNM as compared to FNM.

5.2. Crack propagation examples

After verifying the accuracy and convergence properties of SFNM for static crack problems under mode-I and mode-II loading conditions, here we extend it for simulating the crack propagation problems. Three 2D problems are considered in this section for verifying the accuracy of the proposed SFNM. In the first problem, an edge crack plate is simulated under mode-I cyclic loading. In the second problem, an edge crack plate is considered under mode-II cyclic loading. Finally, a plate with a bi-material interfacial edge crack is simulated under mode-I cyclic loading.

5.2.1. Plate with an edge crack under tensile loading

In this section, we revisit the problem of an edge crack as mentioned in Section 5.1.1 under cyclic loading condition. The initial crack length is considered as $\frac{a}{W} = 0.2$. The crack is considered to propagate under mode-I condition and analysed in the range of $\frac{a}{W} = 0.2$ to $\frac{a}{W} = 0.6$. The plate is subjected to a tensile load of intensity $\sigma = 10$ MPa at the top edge of the plate as shown in Fig. 8. The material properties and other geometric conditions are given in Section 5.1.1. It is well known that the numerical results are strongly mesh size dependent, hence a converged uniform initial mesh of 7442 nodes (61 and 122 nodes in x- and y- directions respectively), is adopted for the simulation, refer section 5.1.1 for more detail. To compare the SFNM results, the stress intensity values are also calculated theoretically. Further, the SIF values obtained by SFNM are compared with the analytical (theoretical) solutions. They are found to be in good agreement as shown in Fig. 15. Finally, the normal stress contour plots obtained by smoothed FNM are shown in Fig. 16 for different crack lengths. From the results, it is observed that the SFNM captures the crack propagation behaviour effectively without the requirement of remeshing and additional enrichment terms.

5.2.2. Plate with an edge crack under shear loading

A rectangular plate with an edge crack under pure shear, shown in Fig. 12 is considered for the simulation. The geometry parameters used in the computation are: width $W = 7$ mm, height $H = 16$ mm, initial crack length is taken as $\frac{a}{W} = 0.2$ where a is the crack length. The material properties Young's modulus E and Poisson's ratio ν are taken as 3×10^7 Pa and 0.25 respectively. The specimen is subjected to shear load $\tau = 1MPa$ at the top edge of the plate. A converged initial mesh with 7442 nodes (61 and 122 nodes in x- and y- directions respectively), is considered for the simulation as discussed in section 5.1.2. For the simulations, crack propagation range is taken as $\frac{a}{W} = 0.2$ to $\frac{a}{W} = 0.6$. The SIF values obtained by SFNM using interaction integral approach are plotted against crack length and compared with FEM results, shown in Fig. 17. Further, the stress contour plots obtained through SFNM are also shown in Fig. 18 under pure shear loading. Due to pure shear all three stress components variation is plotted at a crack to width ratio of 0.5.

From these results, it is observed that the SFNM captures the crack propagation behaviour effectively even for the curved crack growth problems. Finally, the crack trajectories obtained through SFNM and FEM are compared in Fig. 19 and found in good agreement.

5.2.3. Bi-materials edge crack under normal load

A bi-material plate of size 50 mm × 100 mm with an interfacial edge crack of initial length $a = 10$ mm ($\frac{a}{W} = 0.2$) is taken for the simulation as shown in Fig. 20(a). The thickness of the plate is assumed to be 1 mm. A tensile load of intensity $\sigma = 50$ MPa is applied at the top edge of the plate, while the bottom edge of the plate is constrained. An initial uniform mesh of 7442 nodes (61 and 122 nodes in x- and y- directions respectively), is taken for simulations. There is a difference in the elastic properties of the two materials on either side of the interface and symmetry is disrupted even though the geometry of the body is symmetric. The material properties of both the base materials are taken from the literature [14] and given in Table 3.

The fracture toughness of the interface is considered higher than both the base materials for simulation purpose, hence the crack may propagate into either of the material depending on their material properties. The computed equivalent SIF (ΔK_{Ieq}) is compared with the local fracture toughness of both materials to determine the crack trajectory. For this purpose, two ratios R_1 and R_2 are calculated as [41],

$$R_1 = \frac{(\Delta K_{Ieq})_{m1}}{(K_{IC})_{m1}} \quad \text{and} \quad R_2 = \frac{(\Delta K_{Ieq})_{m2}}{(K_{IC})_{m2}}$$

where m_1 and m_2 represent material-1 and material-2 respectively. If the $R_1 > R_2$, the crack will propagate into the first material along the predicted angle $\theta = \theta_c$. Otherwise, it will propagate into the second material.

The obtained crack path through SFNM is compared with the literature in Fig. 20(b). Further, the obtained SIF values using SFNM are compared with the literature results and a good agreement is obtained as shown in Fig. 21. The angle of crack propagation is computed using the maximum circumferential stress theory as discussed in Section 4. The advancement of crack divides the element into several sub-elements. The final deformed configuration at enlarged scale along with sub-elements is depicted in Fig. 22. A small portion of the growth path is magnified and shown in the same figure to illustrate the split and transition elements. From the zoomed view, it can be observed that some of the sub-elements in the split element and transition element maintain poor aspect ratio, lead to error during integration and may deteriorate the convergence rate in FNM. However, in the smoothed FNM such kind of issue does not occur as the domain integral is converted into line integral using the smoothing procedure. The SFNM could be more effective for large deformation problems, where an element distortion is a major problem which reduce the accuracy and convergence rate. The normal stress and normal strain contours at final crack length are shown in Fig. 23.

6. Conclusions

In this work, a smoothed floating node numerical framework for the 2D linear elastic problem is developed by combining FNM with the smoothed FEM. The cell-based smoothening procedure is adopted for the sub-element integration. The proposed framework is easy to implement and can be applied to triangular or quadrilateral or any distorted elements. Field gradients are computed directly using shape functions at midpoints of the boundary segments of the smoothing cells. The combination of SFNM with interaction integral approach offers accurate and path independent evaluation of SIFs. The issue of (sub-)element distortion can be avoided as it does not require the inverse of Jacobian during integration. As a result, SFNM's convergence rate is better than FNM, hence computationally more efficient. From the simulations of this work, it is observed that the SFNM combines the advantages of SFEM and FNM, making it an attractive method for solving fracture mechanics problems.

Declaration of Competing Interest

The authors declare that they have no known competing financial interests or personal relationships that could have appeared to influence the work reported in this paper.

References

[1] T. Belytschko, T. Black, Elastic crack growth in finite elements with minimal remeshing, Int. J. Numer. Methods Eng. 45 (5) (1999) 601–620, https://doi.org/10.1002/(SICI)1097-0207(19990620)45:5<601::AID-NME598>3.0.CO;2-S.

[2] T. Belytschko, L. Gu, Y.Y. Lu, Fracture and crack growth by element free Galerkin methods, Model. Simul. Mater. Sci. Eng. 2 (3A) (1994) 519–534, https://doi.org/10.1088/0965-0393/2/3A/007.

[3] M. Duflot, H. Nguyen-Dang, Fatigue crack growth analysis by an enriched meshless method, J. Comput. Appl. Math. 168 (1-2) (2004) 155–164, https://doi.org/10.1016/j.cam.2003.04.006.

[4] N. Moës, J. Dolbow, T. Belytschko, A finite element method for crack growth without remeshing, Int. J. Numer. Methods Eng. 46 (1999) 131–150, doi: 10.1002/(SICI)1097-0207(19990910)46:1<131::AID-NME726>3.0.CO;2-J.

[5] T. Belytschko, N. Moës, S. Usui, C. Parimi, Arbitrary discontinuities in finite elements, Int. J. Numer. Methods Eng. 50 (2001) 993–1013, doi: 10.1002/1097-0207(20010210)50:4<993::AID-NME164>3.0.CO;2-M.

[6] N. Sukumar, D.L. Chopp, N. Moës, T. Belytschko, Modeling holes and inclusions by level sets in the extended finite-element method, Comput. Methods Appl. Mech. Eng. 190 (46-47) (2001) 6183–6200, https://doi.org/10.1016/S0045-7825(01)00215-8.

[7] T. Rabczuk, G. Zi, A. Gerstenberger, W.A. Wall, A new crack tip element for the phantom-node method with arbitrary cohesive cracks, Int. J. Numer. Methods Eng. 75 (5) (2008) 577–599, https://doi.org/10.1002/nme.v75:510.1002/nme.2273.

[8] T. Chau-Dinh, G. Zi, P.S. Lee, T. Rabczuk, J.H. Song, Phantom-node method for shell models with arbitrary cracks, Comput. Struct. 92–93 (2012) 242–256, https://doi.org/10.1016/j.compstruc.2011.10.021.

[9] A.M. Yan, H. Nguyen-Dang, Multiple-cracked fatigue crack growth by BEM, Comput. Mech. 16 (5) (1995) 273–280, https://doi.org/10.1007/BF00350716.

[10] X. Yan, A boundary element modeling of fatigue crack growth in a plane elastic plate, Mech. Res. Commun. 33 (4) (2006) 470–481, https://doi.org/10.1016/j.mechrescom.2005.06.006.

[11] E. De Luycker, D.J. Benson, T. Belytschko, Y. Bazilevs, M.C. Hsu, X-FEM in isogeometric analysis for linear fracture mechanics, Int. J. Numer. Methods Eng. 87 (6) (2011) 541–565, https://doi.org/10.1002/nme.3121.

[12] D.J. Benson, Y. Bazilevs, E. De Luycker, M.-C. Hsu, M. Scott, T.J.R. Hughes, T. Belytschko, A generalized finite element formulation for arbitrary basis functions: from isogeometric analysis to XFEM, Int. J. Numer. Methods Eng. 83 (6) (2010) 765–785, https://doi.org/10.1002/nme.v83:610.1002/nme.2864.

[13] B.Y. Chen, S.T. Pinho, N.V. De Carvalho, P.M. Baiz, T.E. Tay, A floating node method for the modelling of discontinuities in composites, Eng. Fract. Mech. 127 (2014) 104–134, https://doi.org/10.1016/j.engfracmech.2014.05.018.

[14] S. Kumar, Y. Wang, L.H. Poh, B. Chen, Floating node method with domain-based interaction integral for generic 2D crack growths, Theor. Appl. Fract. Mech. 96 (2018) 483–496, https://doi.org/10.1016/j.tafmec.2018.06.013.

[15] R.H.J. Peerlings, R. de Borst, W.A.M. Brekelmans, M.G.D. Geers, Gradient-enhanced damage modelling of concrete fracture, Mech. Cohesive-Frictional Mater. 3 (1998) 323–342, doi: 10.1002/(SICI)1099-1484(1998100)3:4<323::AID-CFM51>3.0.CO;2-Z.

[16] L.H. Poh, G. Sun, Localizing gradient damage model with decreasing interactions, Int. J. Numer. Methods Eng. 110 (6) (2017) 503–522, https://doi.org/10.1002/nme.v110.610.1002/nme.5364.

[17] A. Negi, S. Kumar, L.H. Poh, A localizing gradient damage enhancement with micromorphic stress-based anisotropic nonlocal interactions, Int. J. Numer. Methods Eng. 121 (18) (2020) 4003–4027, https://doi.org/10.1002/nme.6397.

[18] A. Negi, U. Singh, S. Kumar, Structural size effect in concrete using a micromorphic stress-based localizing gradient damage model, Eng. Fract. Mech. 243 (2021), 107511, https://doi.org/10.1016/j.engfracmech.2020.107511.

[19] B. Bourdin, G.A. Francfort, J.-J. Marigo, Numerical experiments in revisited brittle fracture, J. Mech. Phys. Solids. 48 (4) (2000) 797–826, https://doi.org/10.1016/S0022-5096(99)00028-9.

[20] C. Miehe, F. Welschinger, M. Hofacker, Thermodynamically consistent phase-field models of fracture: variational principles and multi-field FE implementations, Int. J. Numer. Methods Eng. 83 (2010) 1273–1311, https://doi.org/10.1002/nme.2861.

[21] M.J. Borden, T.J.R. Hughes, C.M. Landis, A. Anvari, I.J. Lee, A phase-field formulation for fracture in ductile materials: finite deformation balance law derivation, plastic degradation, and stress triaxiality effects, Comput. Methods Appl. Mech. Eng. 312 (2016) 130–166, https://doi.org/10.1016/j.cma.2016.09.005.

[22] T. Belytschko, Y.Y. Lu, L. Gu, Crack propagation by element-free Galerkin methods, Eng. Fract. Mech. 51 (2) (1995) 295–315, https://doi.org/10.1016/0013-7944(94)00153-9.

[23] S. Kumar, I.V. Singh, B.K. Mishra, A multigrid coupled (FE-EFG) approach to simulate fatigue crack growth in heterogeneous materials, Theor. Appl. Fract. Mech. 72 (2014) 121–135, https://doi.org/10.1016/j.tafmec.2014.03.005.

[24] R.E. Carlson, T.A. Foley, Interpolation of track data with radial basis methods, Comput. Math. with Appl. 24 (12) (1992) 27–34, https://doi.org/10.1016/0898-1221(92)90169-I.

[25] Y. Xu, S. Saigal, Element free galerkin study of steady quasi-static crack growth in plane strain tension in elastic-plastic materials, Comput. Mech. 22 (1998) 255–265, https://doi.org/10.1007/s004660050358.

[26] G.J. Wagner, W.K. Liu, Application of essential boundary conditions in mesh-free methods: a corrected collocation method, Int. J. Numer. Methods Eng. 47 (2000) 1367–1379, doi: 10.1002/(SICI)1097-0207(20000320)47:8<1367::AID-NME822>3.0.CO;2-Y.

[27] M.S. Ingber, C.S. Chen, J.A. Tanski, A mesh free approach using radial basis functions and parallel domain decomposition for solving three-dimensional diffusion equations, Int. J. Numer. Methods Eng. 60 (13) (2004) 2183–2201, https://doi.org/10.1002/nme.v60:1310.1002/nme.1043.

[28] G.R. Liu, Y.T. Gu, Boundary meshfree methods based on the boundary point interpolation methods, Eng. Anal. Bound. Elem. 28 (2004) 475–487, https://doi.org/10.1016/S0955-7997(03)00101-2.

[29] G.R. Liu, Y.T. Gu, An introduction to meshfree methods and their programming (2005), doi: 10.1007/1-4020-3468-7.

[30] G.R. Liu, An overview on meshfree methods: for computational solid mechanics, Int. J. Comput. Methods. 13 (05) (2016) 1630001, https://doi.org/10.1142/S0219876216300014.

[31] J.M. Melenk, I. Babuška, The partition of unity finite element method: basic theory and applications, Comput. Methods Appl. Mech. Eng. 139 (1-4) (1996) 289–314, https://doi.org/10.1016/S0045-7825(96)01087-0.

[32] I. Babuška, Z. Zhang, The partition of unity method for the elastically supported beam, Comput. Methods Appl. Mech. Eng. 152 (1-2) (1998) 1–18, https://doi.org/10.1016/S0045-7825(97)00231-4.

[33] N. Moës, T. Belytschko, Extended finite element method for cohesive crack growth, Eng. Fract. Mech. 69 (7) (2002) 813–833, https://doi.org/10.1016/S0013-7944(01)00128-X.

[34] M. Stolarska, D.L. Chopp, N. Mos, T. Belytschko, Modelling crack growth by level sets in the extended finite element method, Int. J. Numer. Methods Eng. 51 (2001) 943–960, https://doi.org/10.1002/nme.201.

[35] N. Sukumar, Z.Y. Huang, J.-H. Prévost, Z. Suo, Partition of unity enrichment for bimaterial interface cracks, Int. J. Numer. Methods Eng. 59 (8) (2004) 1075–1102, https://doi.org/10.1002/nme.v59:810.1002/nme.902.

[36] L.F. Kawashita, A. Bedos, S.R. Hallett, Modelling mesh independent transverse cracks in laminated composites with a simplified cohesive segment method, Comput. Mater. Contin. 32 (2012) 133–158, https://doi.org/10.3970/cmc.2012.032.133.

[37] S. Kumar, I.V. Singh, B.K. Mishra, K. Sharma, I.A. Khan, A homogenized multigrid XFEM to predict the crack growth behavior of ductile material in the presence of microstructural defects, Eng. Fract. Mech. 205 (2019) 577–602, https://doi.org/10.1016/j.engfracmech.2016.03.051.

[38] S. Kumar, A.S. Shedbale, I.V. Singh, B.K. Mishra, Elasto-plastic fatigue crack growth analysis of plane problems in the presence of flaws using XFEM, J. Contemp. Phys. 50 (2015) 420–440, https://doi.org/10.1007/s11709-015-0305-y.

[39] S. Kumar, G. Bhardwaj, A new enrichment scheme in XFEM to model crack growth behavior in ductile materials, Theor. Appl. Fract. Mech. 96 (2018) 296–307, https://doi.org/10.1016/j.tafmec.2018.05.008.

[40] L. Wen, R. Tian, Improved XFEM: accurate and robust dynamic crack growth simulation, Comput. Methods Appl. Mech. Eng. 308 (2016) 256–285, https://doi.org/10.1016/j.cma.2016.05.013.

[41] S. Bhattacharya, I.V. Singh, B.K. Mishra, T.Q. Bui, Fatigue crack growth simulations of interfacial cracks in bi-layered FGMs using XFEM, Comput. Mech. 52 (4) (2013) 799–814, https://doi.org/10.1007/s00466-013-0845-8.

[42] I.V. Singh, B.K. Mishra, S. Bhattacharya, XFEM simulation of cracks, holes and inclusions in functionally graded materials, Int. J. Mech. Mater. Des. 7 (3) (2011) 199–218, https://doi.org/10.1007/s10999-011-9159-1.

[43] C. Comi, S. Mariani, Extended finite element simulation of quasi-brittle fracture in functionally graded materials, Comput. Methods Appl. Mech. Eng. 196 (41-44) (2007) 4013–4026, https://doi.org/10.1016/j.cma.2007.02.014.

[44] N. Vu-Bac, H. Nguyen-Xuan, L. Chen, S. Bordas, P. Kerfriden, R.N. Simpson, G. R. Liu, T. Rabczuk, A node-based smoothed extended finite element method (NS-XFEM) for fracture analysis, C. - Comput. Model. Eng. Sci. 73 (2011) 331–355, https://doi.org/10.3970/cmes.2011.073.331.

[45] S. Kumar, I.V. Singh, B.K. Mishra, A. Singh, New enrichments in XFEM to model dynamic crack response of 2-D elastic solids, Int. J. Impact Eng. 87 (2016) 198–211, https://doi.org/10.1016/j.ijimpeng.2015.03.005.

[46] A. Menk, S.P.A. Bordas, A robust preconditioning technique for the extended finite element method, Int. J. Numer. Methods Eng. 85 (13) (2011) 1609–1632, https://doi.org/10.1002/nme.3032.

[47] T.-P. Fries, A corrected XFEM approximation without problems in blending elements, Int. J. Numer. Methods Eng. 75 (5) (2008) 503–532, https://doi.org/10.1002/nme.2259.

[48] T.J.R. Hughes, J.A. Cottrell, Y. Bazilevs, Isogeometric analysis: CAD, finite elements, NURBS, exact geometry and mesh refinement, Comput. Methods Appl. Mech. Eng. 194 (2005) 4135–4195, https://doi.org/10.1016/j.cma.2004.10.008.

[49] A. Soni, A. Negi, S. Kumar, N. Kumar, An IGA based nonlocal gradient-enhanced damage model for failure analysis of cortical bone, Eng. Fract. Mech. 255 (2021), 107976, https://doi.org/10.1016/j.engfracmech.2021.107976.

[50] J. Gu, T. Yu, L. Van Lich, S. Tanaka, H. Yuan, T.Q. Bui, Crack growth adaptive XIGA simulation in isotropic and orthotropic materials, Comput. Methods Appl. Mech. Eng. 365 (2020), 113016, https://doi.org/10.1016/j.cma.2020.113016.

[51] H. Yuan, T. Yu, T.Q. Bui, Multi-patch local mesh refinement XIGA based on LR NURBS and Nitsche's method for crack growth in complex cracked plates, Eng. Fract. Mech. 250 (2021), 107780, https://doi.org/10.1016/j.engfracmech.2021.107780.

[52] A. Soni, S. Kumar, N. Kumar, Effect of parametric uncertainties on fracture behavior of cortical bone using XIGA, Eng. Fract. Mech. 233 (2020), 107079, https://doi.org/10.1016/j.engfracmech.2020.107079.

[53] A. Hansbo, P. Hansbo, A finite element method for the simulation of strong and weak discontinuities in solid mechanics, Comput. Methods Appl. Mech. Eng. 193 (33-35) (2004) 3523–3540, https://doi.org/10.1016/j.cma.2003.12.041.

[54] J.-H. Song, P.M.A. Areias, T. Belytschko, A method for dynamic crack and shear band propagation with phantom nodes, Int. J. Numer. Methods Eng. 67 (6) (2006) 868–893, https://doi.org/10.1002/nme.1652.

[55] J. Zhi, B.-Y. Chen, T.-E. Tay, Geometrically nonlinear analysis of matrix cracking and delamination in composites with floating node method, Comput. Mech. 63 (2) (2019) 201–217, https://doi.org/10.1007/s00466-018-1591-8.

[56] N.V. De Carvalho, B.Y. Chen, S.T. Pinho, J.G. Ratcliffe, P.M. Baiz, T.E. Tay, Modeling delamination migration in cross-ply tape laminates, Compos. Part A Appl. Sci. Manuf. 71 (2015) 192–203, https://doi.org/10.1016/j.compositesa.2015.01.021.

[57] G.R. Liu, S.S. Quek, Finite element method: a practical course (2003), doi: 10.1016/B978-0-7506-5866-9.X5000-2.

[58] G.R. Liu, T.T. Nguyen, K.Y. Dai, K.Y. Lam, Theoretical aspects of the smoothed finite element method (SFEM), Int. J. Numer. Methods Eng. 71 (8) (2007) 902–930, https://doi.org/10.1002/nme.1968.

[59] G.R. Liu, K.Y. Dai, T.T. Nguyen, A smoothed finite element method for mechanics problems, Comput. Mech. 39 (6) (2007) 859–877, https://doi.org/10.1007/s00466-006-0075-4.

[60] S.P.A. Bordas, T. Rabczuk, N.-X. Hung, V.P. Nguyen, S. Natarajan, T. Bog, D. M. Quan, N.V. Hiep, Strain smoothing in FEM and XFEM, Comput. Struct. 88 (23-24) (2010) 1419–1443, https://doi.org/10.1016/j.compstruc.2008.07.006.

[61] M. Surendran, S. Natarajan, S.P.A. Bordas, G.S. Palani, Linear smoothed extended finite element method, Int. J. Numer. Methods Eng. 112 (12) (2017) 1733–1749, https://doi.org/10.1002/nme.5579.

[62] B.Y. Chen, T.E. Tay, S.T. Pinho, V.B.C. Tan, Modelling the tensile failure of composites with the floating node method, Comput. Methods Appl. Mech. Eng. 308 (2016) 414–442, https://doi.org/10.1016/j.cma.2016.05.027.

[63] J.S. Chen, C.T. Wu, S. Yoon, Y. You, Stabilized conforming nodal integration for Galerkin mesh-free methods, Int. J. Numer. Methods Eng. 50 (2001) 435–466, https://doi.org/10.1002/1097-0207(20010120)50:2<435::AID-NME32>3.0.CO;2-A.

[64] K.Y. Dai, G.R. Liu, T.T. Nguyen, An n-sided polygonal smoothed finite element method (nSFEM) for solid mechanics, Finite Elem. Anal. Des. 43 (11-12) (2007) 847–860, https://doi.org/10.1016/j.finel.2007.05.009.

[65] W. Xie, X. He, J. Wu, Y. Liu, An edge-based smoothed finite element method for 2D mechanics problems, Xibei Gongye Daxue Xuebao/J. Northwest Polytech. Univ. 35 (2017) 7–12.

[66] Z.C. He, G.R. Liu, Z.H. Zhong, X.Y. Cui, G.Y. Zhang, A.G. Cheng, A coupled edge-/face-based smoothed finite element method for structural-acoustic problems, Appl. Acoust. 71 (10) (2010) 955–964, https://doi.org/10.1016/j.apacoust.2010.06.007.

[67] H. Nguyen-Xuan, S. Bordas, H. Nguyen-Dang, Smooth finite element methods: Convergence, accuracy and properties, Int. J. Numer. Methods Eng. 74 (2) (2008) 175–208, https://doi.org/10.1002/nme.v74:210.1002/nme.2146.

[68] Y. Krongauz, T. Belytschko, Consistent pseudo-derivatives in meshless methods, Comput. Methods Appl. Mech. Eng. 146 (3-4) (1997) 371–386, https://doi.org/10.1016/S0045-7825(96)01234-0.

[69] M. Gosz, J. Dolbow, B. Moran, Domain integral formulation for stress intensity factor computation along curved three-dimensional interface cracks, Int. J. Solids Struct. 35 (15) (1998) 1763–1783, https://doi.org/10.1016/S0020-7683(97)00132-7.

[71] S.S. Wang, J.F. Yau, H.T. Corten, A mixed-mode crack analysis of rectilinear anisotropic solids using conservation laws of elasticity, Int. J. Fract. 16 (3) (1980) 247–259, https://doi.org/10.1007/BF00013381.